

A direct numerical investigation of two-way interactions in a particle-laden turbulent channel flow

Cheng Peng^{1,2}, Orlando M. Ayala³ and Lian-Ping Wang^{1,2,†}

¹Department of Mechanics and Aerospace Engineering, Southern University of Science and Technology, Shenzhen 518055, Guangdong, China

²Department of Mechanical Engineering, University of Delaware, Newark, DE 19716, USA

³Department of Engineering Technology, Old Dominion University, Norfolk, VA 23529, USA

(Received 2 February 2019; revised 18 June 2019; accepted 18 June 2019;
first published online 26 July 2019)

Understanding the two-way interactions between finite-size solid particles and a wall-bounded turbulent flow is crucial in a variety of natural and engineering applications. Previous experimental measurements and particle-resolved direct numerical simulations revealed some interesting phenomena related to particle distribution and turbulence modulation, but their in-depth analyses are largely missing. In this study, turbulent channel flows laden with neutrally buoyant finite-size spherical particles are simulated using the lattice Boltzmann method. Two particle sizes are considered, with diameters equal to 14.45 and 28.9 wall units. To understand the roles played by the particle rotation, two additional simulations with the same particle sizes but no particle rotation are also presented for comparison. Particles of both sizes are found to form clusters. Under the Stokes lubrication corrections, small particles are found to have a stronger preference to form clusters, and their clusters orientate more in the streamwise direction. As a result, small particles reduce the mean flow velocity less than large particles. Particles are also found to result in a more homogeneous distribution of turbulent kinetic energy (TKE) in the wall-normal direction, as well as a more isotropic distribution of TKE among different spatial directions. To understand these turbulence modulation phenomena, we analyse in detail the total and component-wise volume-averaged budget equations of TKE with the simulation data. This budget analysis reveals several mechanisms through which the particles modulate local and global TKE in the particle-laden turbulent channel flow.

Key words: particle/fluid flow, turbulence simulation, multiphase flow

1. Introduction

Understanding how turbulent flows are modified by particles/droplets is of crucial importance to a variety of natural and engineering applications. Examples include sand/dust storm formation, air–sea interactions, soil and coastal erosion, sediment dynamics, petroleum transport in gas pipelines, coal combustion, chemical

† Email address for correspondence: lwang@udel.edu

processing and many others. Early investigations of the two-way interactions between solid particles and turbulent flows took place in the 1960s when a series of experimental measurements were conducted to discover a particle-size dependence of the modulation of turbulent intensities (see reviews of Gore & Crowe 1989; Tanaka & Eaton 2008). These experimental investigations reached a general conclusion that large particles tend to increase turbulence while small particles attenuate turbulence.

While the particle size has been recognized as one of the key parameters in qualifying the turbulence modulation, in the early days, most investigations were focused on particles with sizes smaller than the Kolmogorov length, η , of the carrier fluid turbulence; these particles are also known as point particles. This is because back then there was no technique, in either experimental measurements or numerical simulations, that could resolve directly the disturbance flow around particles accurately and efficiently. Turbulence attenuation was more often reported in these early investigations with small particles, i.e. $d_p < \eta$, where d_p is the particle diameter (see Elghobashi & Truesdell 1993; Kulick, Fessler & Eaton 1994; Paris 2001; Kussin & Sommerfeld 2002; Ferrante & Elghobashi 2003, among many others). This is perhaps because the $d_p < \eta$ condition on particle size leads to the regime where the attenuation mechanisms dominate (Ferrante & Elghobashi 2003). In this regime, the particle effect on the fluid turbulence is described through an additional term $\langle f_i u_i \rangle$ in the turbulent kinetic energy (TKE) budget equation, where f_i is the force exerted by the particles per unit volume, u_i is the undisturbed local fluid velocity and $\langle \dots \rangle$ represents the ensemble averaging (Squires & Eaton 1990; Kulick *et al.* 1994; Li *et al.* 2001). For heavy point particles, the particle force is typically reduced to the Stokes drag (Maxey & Riley 1983). Then $f_i = -\phi_m(u_i - v_i)\delta(\mathbf{x} - \mathbf{Y})/\tau_p$, where v_i is the particle velocity, τ_p is the particle response time, ϕ_m is the particle mass fraction and $\delta(\mathbf{x} - \mathbf{Y})$ is a regularized delta function centred on the particle position \mathbf{Y} . Neglecting the delta function, a simplified approximation of the two-way coupling force is $f_i = -\phi_m(u_i - v_i)/\tau_p$, then the two-way coupling term applied to the fluid kinetic energy equation is expressed approximately as $\langle f_i u_i \rangle = \langle -\phi_m(u_i - v_i)u_i/\tau_p \rangle$. Assuming ϕ_m is known and applying the Reynolds decomposition, the part of the coupling term in the TKE equation reads $\langle -u'_i u'_i + u'_i v'_i \rangle \phi_m/\tau_p$. When the particle and fluid velocity fluctuations are of the same order of magnitude, the ensemble average of particle-to-fluid correlation $\langle u'_i v'_i \rangle$ is usually smaller than the fluid-to-fluid correlation $\langle u'_i u'_i \rangle$, thus $\langle -u'_i u'_i + u'_i v'_i \rangle \phi_m/\tau_p$ is typically negative and acts as an additional dissipation to TKE. Vreman (2015) added constant inhomogeneous force fields, resulting from the particles, to a single-phase turbulent channel flow and found significant turbulence attenuation. This indicates that the mean part of the particle force could also play a role in turbulence modulation under certain flow configurations. The mechanism possibly acts to modify the energy transfer from the mean flow to the turbulent fluctuations.

However, the above identified mechanisms only provide an incomplete picture of the turbulence modulation. When the particles are of finite size, they also bring in disturbance and discontinuity to the fluid phase, which makes the above analysis no longer applicable (Eaton 2009; Tanaka & Eaton 2010). For example, the particle-induced vortex shedding has been recognized as an important mechanism contributing to the enhancement of the turbulence (Kajishima *et al.* 2001; Balachandar & Eaton 2010; Botto & Prosperetti 2012). The disturbance flows are associated with the no-slip boundary condition on particle surfaces, which is not fully considered in the above simple analysis.

In recent years, rapid developments of computers and simulation methods have enabled fully resolved simulations (FRSs) of turbulent particle-laden flows, see reviews

by Tenneti & Subramaniam (2014) and Maxey (2017). FRSs provide a great opportunity to advance our current understanding of turbulence modulation. Compared to the Lagrangian point-particle simulations, the resolved fluid–particle interfaces provide the correct flow details around the particles (Lucci, Ferrante & Elghobashi 2010; Botto & Prosperetti 2012). The direct numerical simulations also allow full access to the flow data at all scales. Turbulence modulations in homogeneous isotropic turbulence (HIT) were extensively studied by FRSs during the past decade (see Burton & Eaton 2005; Lucci *et al.* 2010; Botto & Prosperetti 2012; Gao, Li & Wang 2013; Vreman 2016; Brändle de Motta *et al.* 2016, among many others). Regions with significantly enhanced dissipation rate around the particles were directly observed in those FRSs, which were recognized as one of the major mechanisms resulting in turbulence attenuations. Lucci *et al.* (2010) investigated the two-way coupling effect in their FRS of a decaying HIT based on an immersed boundary method (IBM). They found that the boundary force f_i obtained from IBM and the fluid velocity near the particle surfaces u_i had the preference to align in the same direction, thus the statistical average of the coupling term $\langle f_i u_i \rangle$ was positive, which may act as a turbulence augmentation mechanism. Vreman (2016) conducted a TKE budget analysis for the flow around static particles in a forced HIT. The net transport of TKE towards the particle surfaces was discovered. A simple TKE dissipation rate $(k - \varepsilon)$ analysis over the whole flow is not sufficient to reveal a local picture of turbulence modulation introduced by particles. It is worth noting that the above studies all assumed homogeneity and isotropy in the carrier turbulence. In a wall-bounded turbulent flow that is inhomogeneous and anisotropic, the presence of particles is found to result in different levels of modifications to the turbulent kinetic energy of different velocity components, and at different wall-normal locations (Kulick *et al.* 1994; Kussin & Sommerfeld 2002). This implies that the presence of particles also directly affects the transport and inter-component exchange of TKE. In these cases, turbulence modulation becomes a more complex phenomenon far from being understood, especially when $d_p > \eta$.

The first FRS of particle-laden turbulent channel flow was reported by Pan & Banerjee (1997), where the flow modulation by a few dozen finite-size particles in a horizontal open channel flow was investigated. Their simulation involved two different sizes of both fixed and freely moving particles. The largest enhancement was observed with the large-size fixed particles. This enhancement was found to result from vortex shedding on the particle surfaces. A similar turbulence augmentation in a vertical channel flow due to vortex shedding was reported by Kajishima *et al.* (2001). The particle Reynolds number in the simulation was approximately $Re_p = Ud_p/\nu = 500$, where U is the terminal settling velocity of the particle, d_p is the particle diameter, ν is the fluid viscosity. Uhlmann (2008) performed a closely related study of heavy particles in a vertical turbulent channel flow, at a particle Reynolds number of approximately 136 which might not be sufficient to trigger vortex shedding events. However, an enhanced TKE was still observed, but component-wise, only the streamwise TKE was found increased, the wall-normal and spanwise TKE were reduced.

Recently, more FRSs of horizontal channel flows (Shao, Wu & Yu 2012; Picano, Breugem & Brandt 2015; Costa *et al.* 2016; Wang *et al.* 2016b; Eshghinejadfard *et al.* 2017; Yu *et al.* 2017) and pipe flows (Wu, Shao & Yu 2011; Gupta, Clercx & Toschi 2018; Peng & Wang 2018) were reported, as more efficient no-slip boundary treatments on particle surfaces were developed. These independent investigations applied different numerical methods but some similar observations were reached.

For example, with the presence of neutrally buoyant particles, more homogeneous TKE distribution along the wall-normal direction and a more isotropic distribution of TKE among three velocity components, compared to the single-phase counterpart, were observed. How the flow is modulated by the dispersed phase with different levels of volume fraction, particle size, particle inertia, etc. is another focus of these recent studies. Shao *et al.* (2012) employed two particle sizes in their simulations and reported that, at a constant particle volume fraction, small particles induced larger modulation to both the mean flow velocity and TKE due to a larger total surface area. A same observation was made by Eshghinejadfard *et al.* (2017). Picano *et al.* (2015) studied the flow modulation in a horizontal turbulent channel flow with varying particle volume fractions. An augmented turbulent intensity was reported at small particle volume fractions but when the particles become dense (20% particle volume fraction), the turbulent intensity was actually decreased. Costa *et al.* (2016) analysed the profiles of mean flow velocity in the turbulent channel flow with dense particle suspensions. They argued that there was a unified log law applied to both the single-phase and particle-laden turbulent channel flows, using a rescaling based on the effective viscosity of homogeneous suspension and the effective distance from a virtual wall formed by dense particle concentration. Yu *et al.* (2017) investigated the effects of the particle/fluid density ratio on flow modulation. They found that the modulation of mean flow velocity did not monotonically change with the particle/fluid density ratio; the maximum reduction of the flow speed occurred at a density ratio of approximately 10, while both smaller and larger density ratios induced a smaller reduction in the mean flow speed. On the other hand, turbulence intensity was increased with increasing the particle/fluid density ratio. While these FRSs contributed significantly in providing qualitative picture of the turbulent modulation and its parameter dependence, efforts in identifying the flow modulation mechanisms and quantifying their impacts were still largely missing.

In this study, we aim at conducting a more quantitative analysis of various specific turbulence modulation processes brought by finite-size particles at the mechanistic level. The main approach is to perform a thorough energy budget analysis based on our FRS data of particle-laden turbulent channel flows, in order to reveal the mechanisms responsible for the flow modulations, the levels of modulation and specific roles of particle rotation. Attention will be given to the distribution of particles in the turbulent channel flow and its impact on the modulations of the mean flow and turbulence. In particular, detailed budget analyses of the stress balance and the TKE balance will be conducted to provide insights into how particles modulate turbulent flows through multiple mechanisms.

The paper is structured as follows. In § 2, we will briefly introduce the numerical method, which is the lattice Boltzmann method, and detailed simulation set-ups. In § 3, two simple cases, a spherical particle settling in a quiescent flow and the bouncing of a single particle from a flat wall, will be examined first to validate the simulation method. The simulation results will be discussed and analysed in § 4. Finally, major conclusions from the present study will be recapitulated in § 5.

2. Problem description and numerical method

Figure 1 shows a snapshot of a turbulent channel flow laden with a number of neutrally buoyant, monodisperse, finite-size particles, at its statistical stationary state. The size of the channel is $L_x \times L_y \times L_z = 12H \times 2H \times 4H$, where H is the half-channel width. The background flow is driven by a constant pressure gradient

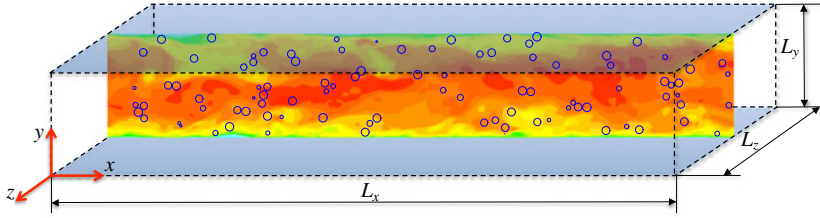


FIGURE 1. (Colour online) A snapshot of a particle-laden turbulent channel flow at the statistical stationary state.

Case #no.	$L_x \times L_y \times L_z$	Re_τ	$\delta x/y_\tau$	d_p/H	d_p/y_τ	N_p	Φ_p	ρ_p/ρ_f
SP	$12H \times 2H \times 4H$	180	1.204	—	—	—	—	—
PLL(PLL–NR)	$12H \times 2H \times 4H$	180	1.204	0.161	28.90	2231	5%	1.0
PLS(PLS–NR)	$12H \times 2H \times 4H$	180	1.204	0.080	14.45	17 845	5%	1.0

TABLE 1. Key physical parameters used in the simulations.

$-dp/dx = \rho g$ along the streamwise direction to maintain a friction Reynolds number $Re_\tau = u_\tau H/\nu = 180$, where u_τ is the friction velocity, ν is the fluid kinematic viscosity. Mono-dispersed, neutrally buoyant particles of two different sizes are released into the background flow to establish two particle-laden channel flow simulations. In order to avoid strong and sudden perturbations to the flow that may cause numerical instability, particles are inserted into the background flow as small seeds, growing up gradually to their final sizes over a period of approximately one eddy turnover time ($T_e = H/u_\tau$). Five different simulations were performed in the present study. The first one is the single-phase (SP) turbulent channel flow which serves as a reference case. For the particle-laden simulations (PL), two particle sizes are studied: the small-size case (PLS) and the large-size case (PLL). For comparison purposes, two additional runs are conducted, without particle rotation (NR), i.e. particles are only allowed to have translational motion, but not allowed to rotate. The total particle volume fraction $\Phi_p = (N_p \pi d_p^3/6)/(L_x L_y L_z)$ in each particle-laden case is set to 5%, where N_p is the number of particles, d_p is the particle diameter. For all cases simulated, the local volumetric driving force $\rho g L_x L_y L_z$ is fixed, namely, the same body force is applied in the fluid phase and inside solid particles. We have summarized the key parameters used in the five simulations in table 1.

Simulations of the current study are conducted using the lattice Boltzmann method (LBM). Different from most of the previous LBM studies of particle-laden turbulent flows using the D3Q19 lattice grid (e.g. Ten Cate *et al.* 2004; Gao *et al.* 2013; Eshghinejadfard *et al.* 2017), the present fluid flow simulations are carried out by the multiple-relaxation time (MRT) lattice Boltzmann (LB) model based on a D3Q27 (three-dimensional twenty-seven discrete velocity) lattice grid. This is in light of our recent finding that the D3Q27 lattice yields a better numerical stability than the D3Q19 lattice when the other conditions are the same. More details of the MRT-LB model used in the present study can be found in our recent publications (Peng *et al.* 2018; Peng & Wang 2018). A uniform cubic mesh is used in all cases, where the spatial grid resolution is chosen as $H = 149.5\delta x$, which transfers to $\delta x/y_\tau = 1.204$, $\delta x = \delta y = \delta z$. Here $y_\tau = \nu/u_\tau$ is the wall unit, which is the characteristic length in the

viscous sublayer. From the established direct numerical simulation (DNS) database, with a friction Reynolds number $Re_\tau = 180$, the size of the smallest eddies, which is the Kolmogorov length, is $\eta \approx 1.5y_\tau$ (Lammers *et al.* 2006). It should be noted that this Kolmogorov length is calculated with the averaged dissipation rate at the wall. Due to the intermittent nature of a turbulent flow, the instantaneous and local dissipation rate could be larger, which could result in a smaller Kolmogorov length that requires a finer grid resolution. In the present LBM simulations, the first layer of grid points in the wall-normal direction is located half of a grid spacing from the channel wall. Another criterion for selecting the grid resolution is the need to resolve the flow in the boundary layer on the particle surface. The boundary layer thickness around a particle can be roughly estimated as $\delta \approx d_p/\sqrt{Re_p}$ (Xu & Subramaniam 2010). In the present simulations, since the particles move with the flow, the relative velocity between a particle and the flow phase around should be relatively small.

As we will observe later in §4.1, in most of the region the particle Reynolds number $Re_p = |U_f^+ - U_p^+|d_p^+$ is no larger than 30. This leads to boundary layer thicknesses of $\delta \approx 5.28y_\tau$ and $\delta \approx 2.64y_\tau$ for large and small-size particles, respectively, which is larger than the grid resolution ($\delta x = 1.204y_\tau$) in the simulations. We have also performed some investigations of the necessary grid resolution in laminar flows. For particle Reynolds numbers $Re_p = 20, 50$ and 150 , the grid resolutions to achieve a less than 1% relative error in the drag coefficient are $d_p = 14.3\delta x, 16.7\delta x$ and $15.9\delta x$, respectively. In this study, the large and small particle cases are simulated with $d_p = 24\delta x$ and $d_p = 12\delta x$, respectively. Based on these arguments, the grid resolution adopted in the present study should be viewed as reasonably adequate for most of the flow and particle statistics to be discussed later in this paper, except a small region very close to the channel walls.

The treatment of the no-slip boundary condition on the moving particle surfaces is based on the interpolated bounce back schemes (see Bouzidi, Firdaouss & Lallemand 2001; Zhao & Yong 2017). The unknown distribution functions at a boundary node are directly constructed from the known ones, such that the no-slip velocity constraints are satisfied with a second-order accuracy. With the interpolated bounce-back schemes, the interfaces between the fluid and particle phases remain sharp, so the numerical dissipation associated with the boundary treatment is very small. In particular, the quadratic interpolated bounce-back scheme proposed by Bouzidi *et al.* (2001) is adopted as the default scheme for treating the no-slip boundary condition on moving particle surfaces. To implement this scheme requires up to two other node points besides the boundary node itself on the fluid side (Bouzidi *et al.* 2001). When two particles are very close, this condition may not be met. In this situation, the linear interpolated bounce-back scheme by Bouzidi *et al.* (2001) that requires only one extra node point on the fluid side and the single-node second-order bounce-back scheme by Zhao & Yong (2017) that requires no extra node point are employed successively. These schemes all possess a second-order accuracy by design, so the overall second-order accuracy of the velocity field can be maintained. The schemes involve more node points are found to be more accurate (in terms of absolute values of the error) and robust (Peng *et al.* 2016). Thus they are applied first when the condition allows. A Galilean invariant momentum exchange method is applied to calculate the hydrodynamic force and torque acting on each particle (Wen *et al.* 2014; Peng *et al.* 2016). In the present simulations, the volumes occupied by the particles contain no fluid information. When a node point that was previously covered by a solid particle becomes a fluid node point, the distribution functions at this fresh node need to be initialized. Here the ‘equilibrium + non-equilibrium’ refilling scheme

by Caiazzo (2008) is chosen. The performances of the aforementioned schemes are extensively validated in a series of laminar flow problems (Peng *et al.* 2016; Tao, Hu & Guo 2016) and several turbulent flow simulations (Wang *et al.* 2016c; Peng & Wang 2018). In § 3, we will provide another two validation tests to confirm their capability.

The average particle volume fraction in the present particle-laden cases is fixed at $\Phi_p = 5\%$. This is above the dilute limit ($\Phi_p \leq 0.1\%$). In this circumstance, the particle–particle and particle–wall interactions must be considered. There are two categories of the lubrication model to handle the unresolved short-range hydrodynamic interactions that have been constantly used in FRSs. The first category is the repulsive barriers (in e.g. Uhlmann 2008; Lucci *et al.* 2010; Shao *et al.* 2012; Wang *et al.* 2016a; Eshghinejadfard *et al.* 2017; Uhlmann & Chouippe 2017), which assume the short-range hydrodynamic interactions are always repulsive forces depending only on the gap distance between two approaching solid surfaces. The other category is the Stokes lubrication forces (in e.g. Ten Cate *et al.* 2004; Picano *et al.* 2015; Brändle de Motta *et al.* 2016), which are based on the theoretical lubrication forces in the Stokes flow limit. In this study we choose the Stokes lubrication force model by Breugem (2010) to model the short-range hydrodynamic interactions. The lubrication force is applied in a piecewise manner, as suggested by Brändle de Motta *et al.* (2013), with the coefficients $\epsilon_0 = 0.125$, $\epsilon_1 = 0.001$ and $\epsilon_2 = -0.005$ for inter-particle interactions and $\epsilon_0 = 0.15$, $\epsilon_1 = 0.001$ and $\epsilon_2 = -0.005$ for particle–wall interactions. Here ϵ_0 is the threshold distance below which the hydrodynamic interaction is no longer resolved and the lubrication force model must be activated; ϵ_1 is the threshold below which the lubrication force is maintained constant rather than changing with the actual gap distance between the two solid surfaces. It is introduced to avoid the divergence of the lubrication forces when the gap distances are small. The parameter ϵ_2 is the distance below which the lubrication force is turned off. The values of ϵ_2 are negative, which means the two solid surfaces are in physical contact. In this situation, the hydrodynamic interaction becomes insignificant and the contact force takes over; ϵ_2 is not set to precisely zero because even when the physical contact starts there are still fluids around the contact point that contribute partially to the interaction force.

A soft-sphere collision model proposed by Breugem (2010) is employed when two solid objects are in physical contact to prevent them from generating non-physical overlap. While a realistic contact collision happens extremely fast, in a simulation, we have to allow the collision to happen during multiple time steps so the collision process can be adequately resolved. In this adopted model, we set the collision period $N_c = 8\delta t$, i.e. each collision covers 8 fluid time steps. In addition, a smaller particle time step $dt = 0.2\delta t$, is used to update the particle motion. The dry collision restitution coefficient is set to 0.97 following Brändle de Motta *et al.* (2013). More information about the models for the boundary treatments and the particle–particle, particle–wall interactions can be found in the references given above.

3. Numerical validation of the code

To demonstrate the performance of the numerical method used in the current study, two validation cases are considered in this section. The first case is a spherical particle settling in a quiescent fluid under gravity. The same problem had been experimentally studied by Ten Cate *et al.* (2002), using particle imaging velocimetry (PIV) measurements. The experimental set-up is summarized as follows. The tank has a size of 100 mm \times 160 mm \times 100 mm and its top is a free surface. The particle

	$\rho_f(\text{kg m}^{-3})$	$\mu_f(10^{-3} \text{ Nm s}^{-1})$	Re	τ
Case 1	970	373	1.5	0.9
Case 2	965	212	4.1	0.9
Case 3	962	113	11.6	0.8
Case 4	960	58	32.2	0.65

TABLE 2. Parameters used in the validation simulations of a spherical particle settling in a quiescent fluid.

is made of Nylon, which has a density of $\rho_p = 1120 \text{ kg m}^{-3}$, and a diameter of $d_p = 15 \text{ mm}$. Initially the particle is located at the centre in the x and z directions, and 120 mm from the bottom wall. Four types of silicon oil are used as the working fluid, whose properties are summarized in table 2. The Reynolds numbers listed in table 2 are based on the estimated terminal velocity in each case. The last column of table 2 is the relaxation time used in the LBM simulation, which determines the magnitude of the physical viscosity. The LBM simulations are conducted with a grid resolution of $n_x \times n_y \times n_z = 100 \times 160 \times 100$. This grid resolution is chosen to match the LBM simulations reported in Feng & Michaelides (2005) who used an immersed boundary method (IBM) to treat the no-slip boundary on the particle surface. The relaxation times τ in the last columns of table 2 are also identical to those used by Feng & Michaelides (2005). The velocity in each case is compared with the experimental data from Ten Cate *et al.* (2002) and the updated results from an improved LBM-IBM simulation by Feng & Michaelides (2009) in figure 2. It can be seen that under the same grid resolution, the results of the present simulations based on the interpolated bounce-back schemes are in good agreement with the experimental measurements and the LBM-IBM results.

The second validation case concerns a settling particle bouncing from a flat wall in a viscous fluid. The wet restitution coefficient e_w defined as $|u_2/u_1|$ is investigated, where u_1 and u_2 are magnitudes of the incident and bouncing-back particle velocity, respectively. It is well known from experimental measurements that the wet restitution coefficient e_w can be fitted empirically as a function of the collision Stokes number St_c (Joseph 2003; Legendre *et al.* 2006),

$$\frac{e_w}{e_d} = \exp\left(-\frac{35}{St_c}\right), \quad (3.1)$$

where e_d is the dry restitution coefficient when the fluid is not present, $St_c = \rho_p u_1 d_p / 9 \mu_f$, μ_f is the dynamic fluid viscosity. Following Breugem (2010), u_1 and u_2 are chosen as the maximum values of the incident and bounce-back velocities, respectively. The simulations are conducted in an unconstrained domain with four sides being stress free. The particle to fluid density ratio is fixed to $\rho_p / \rho_f = 8$ and the simulation is conducted with a spatial resolution of $d_p = 16 \delta x$. The fluid viscosity is varied to adjust the particle Stokes number when the particle arrives at the wall. The domain length along the direction of gravity is made long enough so the particle can reach its terminal settling velocity before interacting with the wall. The values of ϵ_0 , ϵ_1 and ϵ_2 in the lubrication force model of Brändle de Motta *et al.* (2013) are chosen as 0.15, 0.001 and -0.01 , respectively, and the dry restitution coefficient e_d is 0.97. To allow a larger particle–fluid density ratio and the presence of gravity here, a different value of ϵ_2 is used in this validation case,

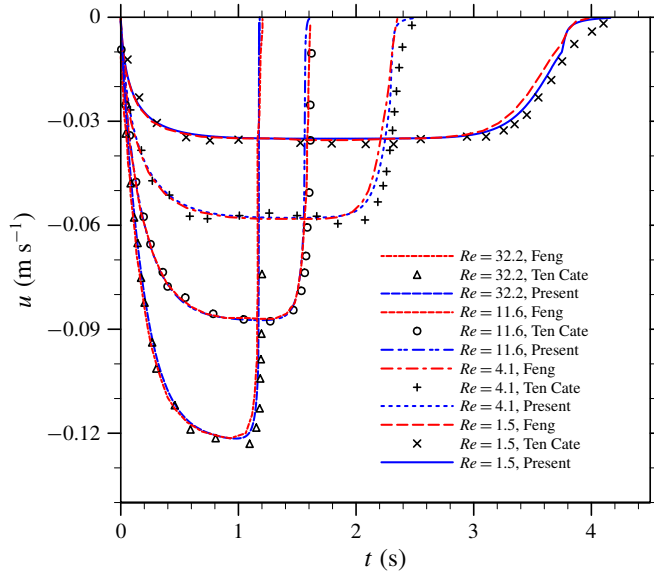


FIGURE 2. (Colour online) Time-dependent particle velocities of a spherical particle settling in a quiescent fluid. The results are compared with the results of LBM-IBM presented later by Feng & Michaelides (2009) because the quality of the results was improved from their earlier simulations.

compared to the particle-laden turbulent flow simulations. In order to better resolve the collision process, the collision period N_c is chosen to be 12, where $dt = 0.1\delta_t$ is used to update the particle motion. These two parameters are also different from the particle-laden turbulent channel flow simulations since the validation simulation is much more computationally affordable, which allows us to use a finer time step size to better resolve the collision process. The wet restitution coefficients at different St_c are shown in figure 3. The lubrication force model and the soft-sphere contact collision model together yield a good prediction of the effects of the unresolved particle–wall interactions on the particle dynamics, and the wet restitution coefficient is accurately simulated. Besides the above two validation cases, the numerical method used in the current study was also compared with the finite-volume-based IBM and Lagrangian volume of fluid (Lag-VOF) method in a decaying homogeneous isotropic particle-laden turbulent flow, as reported recently in Brändle de Motta *et al.* (2019).

4. Results and discussion

The results of turbulent statistics to be shown in this section are both spatially and temporally averaged. By default, the spatial average is conducted over the volume occupied a specific phase, i.e. phase averaged. For example, each data point in the profiles of fluid TKE shown in figure 6 is averaged over a (x, z) (streamwise–spanwise) plane at a given y (wall-normal) location over the grid cells occupied by the fluid phase. The same applies to the profiles of particle TKE shown in the same figure, but the spatial average is conducted over the grid cells occupied by the particles. The spatially averaged results are then averaged over roughly 1500 time frames at the statistical stationary state, which covers approximately 30 eddy turnover times. We use the angle brackets $\langle \dots \rangle$ to denote a quantity that has been phase averaged, and an overbar $\overline{\dots}$ to denote a quantity that has been time averaged.

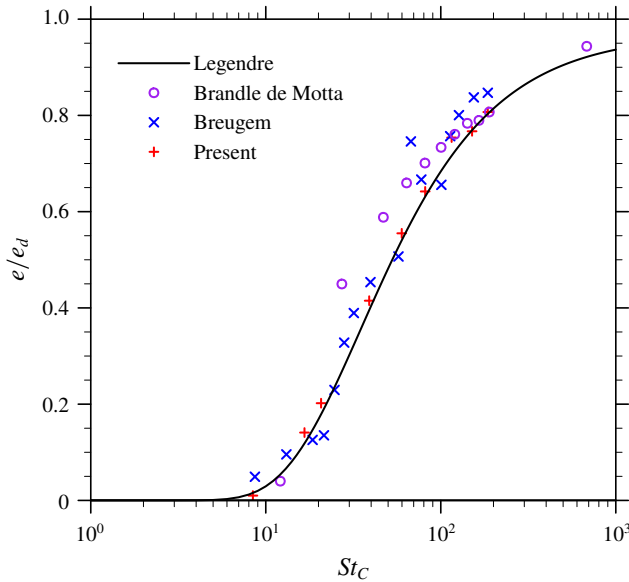


FIGURE 3. (Colour online) The wet restitution coefficients during a particle–wall contact collision as a function of collision Stokes number St_c . The results are compared to the numerical studies of Breugem (2010) and Brändle de Motta *et al.* (2013), and the empirical relation of Legendre *et al.* (2006).

4.1. Particle distribution in a turbulent channel flow

Before moving to the discussion of the turbulent flow statistics, the distribution of solid particles in the turbulent channel flow is investigated first. In the past, the drag and lift forces acting on a fixed finite-size spherical particle in a turbulent channel flow were studied carefully by Zeng *et al.* (2008), but the study of the statistical behaviours of a group of finite-size particles under physical particle–particle lubrication and contact interactions is still largely missing. Clearly, the statistical behaviours of particles should have a significant impact on the flow modulation. First, snapshots of streamwise velocity contour on a cross-sectional plane (x – y plane at $z = L_z/2$), together with the surface positions of particles crossing this plane, are shown in figure 4 for the four particle-laden turbulent channel flows. In all four cases, clusters of particles can be observed. It should be stressed that correct simulations of the clustering requires validated lubrication and contact interaction treatments, as already demonstrated in figure 3.

To quantify the clustering, the particle radial distribution function (RDF) $g(r_i)$, which is defined as $g(r_i) = (N_i/V_i)/(N/V)$, is calculated and presented in figure 5, where N_i is the number of particle pairs separated with a distance in the range of $(r_i - \Delta r, r_i + \Delta r)$, V_i is the shell volume equal to $4\pi[(r_i + \Delta r)^3 - (r_i - \Delta r)^3]/3$, N is the total number of particle pairs $N = N_p(N_p - 1)/2$ and V is the total volume $L_x L_y L_z$. The time-averaged RDF for all four particle-laden cases peak at a centre-to-centre separation distance of $r_i = d_p$. The two small particle cases show higher levels of particle clustering than the large particle cases. When the particle rotation is restricted, the two corresponding cases also exhibit slightly higher peaks of RDF compared to their respective free-rotation counterpart. A second peak of RDF is also present in each case at $r_i = 2d$, which implies the particle can form chain-shaped clusters having

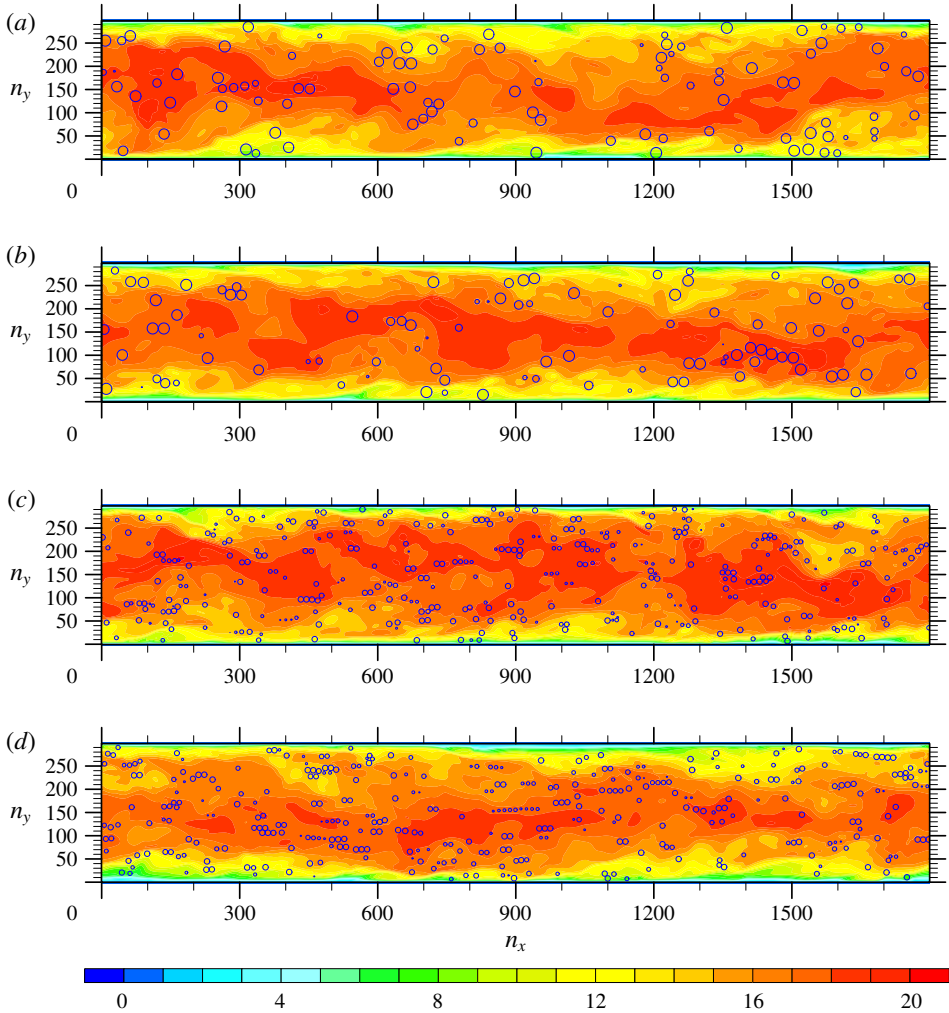


FIGURE 4. (Colour online) Snapshots of streamwise velocity contours and particle surface locations on a cross-section of $z=L_z/2$ at a random time: (a), case PLL, (b) case PLL-NR, (c) case PLS, (d) case PLS-NR.

more than two particles. When $r_i > 2d$, RDF in each case stays around unity. The preferential concentration of particles, i.e. small particles tend to gather in the region with high strain rate and low vorticity, is not obvious for the finite-size particles in the present simulations. This is because the particle sizes in the present simulations are too large to be affected by the small vortices responsible for the preferential concentration. The unit particle-to-fluid density ratio also largely eliminates this inertia bias.

The observation of particle clusters in the present simulations contradicts that reported in the earlier investigation of Uhlmann (2008), where no particle cluster was reported in a particle-laden turbulent flow in a vertical channel. Uhlmann (2008) concluded that the particle Reynolds number ($Re_p \approx 140$) in his simulation was not large enough to trigger strong wake effects to bring particles together, so particle clusters did not form. In the present simulations, the particle Reynolds number

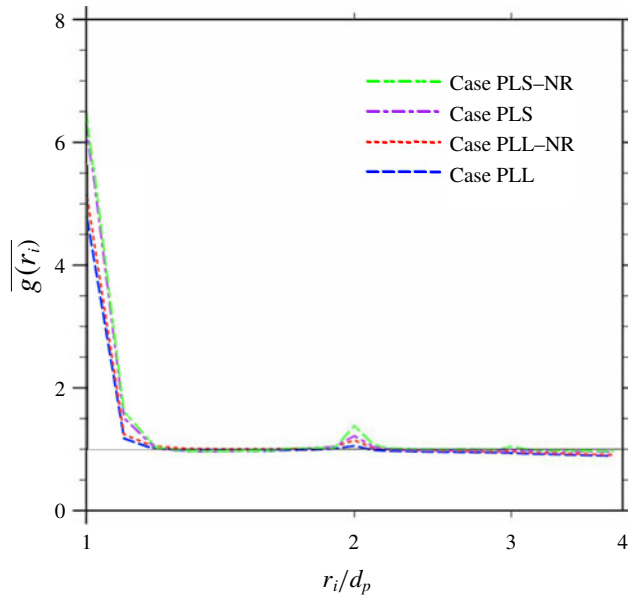


FIGURE 5. (Colour online) The particle radial distribution functions in the present particle-laden turbulent channel flow simulations.

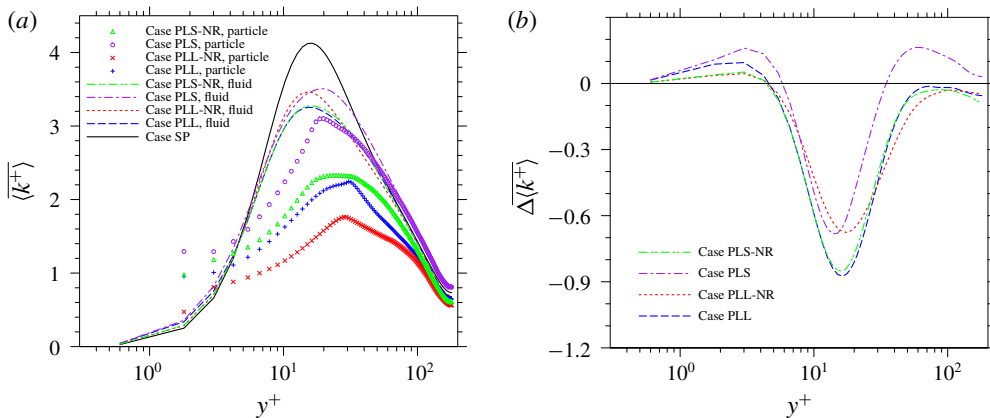


FIGURE 6. (Colour online) The turbulent kinetic energy of the particle and fluid phases in single-phase and particle-laden turbulent channel flows: (a) TKE, (b) relative change from case SP, i.e. $\Delta \langle k^+ \rangle = \overline{\langle k_{pl}^+ \rangle} - \overline{\langle k_{sp}^+ \rangle}$. All results are normalized by the inner scale of the corresponding single-phase simulations.

calculated based on the difference between the fluid and particle mean velocities $Re_p = \|U_f^+ - U_p^+\| d_p^+$ (the superscript + means that a quantity has been normalized by the fraction velocity u_τ and the wall unit y_τ) is no larger than 30 in most regions of the channel except near the channel wall, but the particle clusters are observed at every wall-normal location, as shown in figure 4. It is therefore concluded that particle clustering is not directly caused by the wake effect.

To understand the true reason for particle clustering, we calculate the collision Stokes number $St_c = \rho_p / \rho_f \cdot \Delta U^+ d_p^+ / 9$ with the relative velocity ΔU being estimated

as twice the maximum of the particle root-mean-square (r.m.s.) velocity in the channel. The profiles of turbulent kinetic energy of the fluid and particle phases are given in figure 6. The collision Stokes numbers for a typical inter-particle collision in the case PLL, case PLL–NR, case PLS and case PLS–NR are approximately 14, 12, 8 and 7, respectively. Using the empirical relation between the hydrodynamic interaction Stokes number and the wet restitution coefficient in (3.1) (note that this correlation is for particle–wall collision but the particle–particle collision should have a similar magnitude (Yang & Hunt 2006)), the wet restitution coefficients of inter-particle collisions in case PLL, case PLL–NR, case PLS and case PLS–NR are estimated to be 0.08, 0.05, 0.01 and 0.007, respectively. These low wet restitution coefficients lead to high probabilities for two colliding particles to form a particle cluster. The above argument is very similar to the one made by Brändle de Motta *et al.* (2016) to justify the existence of particle–particle secondary collisions in their particle-laden forced HIT, except that they define the relative velocity ΔU as $\sqrt{32\langle k \rangle}/3\pi$ in HIT. This reasoning is also well supported by the results in figure 5. Small particles form higher levels of particle clusters than large particles due to smaller St_c values. From both figures 5 and 6, particles without rotation are observed to form a higher level of particle clusters than particles which can rotate freely, probably because particle rotation increases relative motion locally at the contact point, which may reduce the hydrodynamic interaction time and as such the rotating particles after a contact collision could separate more easily. This is supported by the large St_c for rotating particles relative to their respective non-rotating case.

There are a few possible explanations for the absence of particle clusters in Uhlmann (2008). One explanation could be that the particles in Uhlmann (2008) were heavy particles, i.e. $\rho_p/\rho_f = 10$ and 2.21, while the particles in the present simulations are neutrally buoyant, $\rho_p/\rho_f = 1$. Heavy particles tend to result in larger collision Stokes numbers and lead to larger wet coefficients of restitution that prevent cluster formation after collisions. Another possible explanation for the different observations on particle clusters could be due to the different lubrication models used to treat the particle–particle interactions. In Uhlmann (2008), the repulsive barrier proposed by Glowinski *et al.* (1999) was used while in the present simulations the Stokes lubrication forces by Brändle de Motta *et al.* (2013) are used. The repulsive barrier always adds a repulsive force between two nearby particles regardless of whether they are approaching or moving apart. This repulsive force prevents particles from forming stable clusters when they approach each other. On the contrary, the Stokes lubrication forces always act to reduce the relative motion and as such favour cluster formation. Similar observations were constantly made in studies of colloidal suspensions with the inclusion of Stokes lubrication forces (see e.g. Brady & Bossis 1988). The Stokes lubrication forces make two interacting particles more difficult to separate and could even lead to multiple secondary collisions. In earlier studies, secondary collisions between particles were reported by Ten Cate *et al.* (2004) and Brändle de Motta *et al.* (2016) when similar lubrication barriers were used.

To further clarify the above point, two comparative simulations, which use identical simulation set-ups to case PLL and case PLS but with a repulsive barrier were conducted. These two comparative simulations are labelled as ‘case PLL–RB’ and ‘case PLS–RB’, ‘RB’ stands for ‘repulsive barrier’, and the repulsive barrier examined here is the one proposed by Feng & Michaelides (2005), which is similar to the one used by Uhlmann (2008) but with a better design to handle the repulsive forces due to short-range hydrodynamic interaction and particle physical contact. The short-range hydrodynamic interaction in this repulsive model is modelled as a

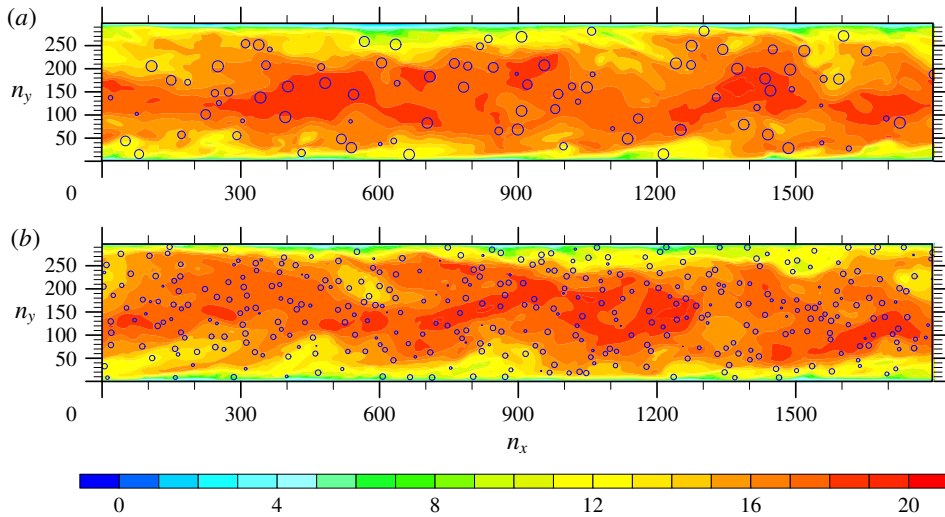


FIGURE 7. (Colour online) Snapshots of streamwise velocity contours and particle surface locations on a cross-section of $z = L_z/2$ at a given time: (a), case PLL-RB, (b) case PLS-RB.

quadratic function of the gap distance, while the contact force is modelled as a spring force based on the overlap distance. Since this model handles both the short-range hydrodynamic interaction and the contact force, the soft-sphere collision model is no longer necessary.

When case PLL-RB and case PLS-RB reach their statistical stationary states, snapshots of the particle locations on a cross-section at $z = L_z/2$ are taken and shown in figure 7. Compared to their counterparts in figure 4(a,c), particle clusters are no longer observed under the repulsive model. RDFs of the particle distribution in the two additional cases shown in figure 8 further confirm this contrast. Instead of forming clusters, slightly higher particle concentrations are identified at $r_i/d_p = 1.2$ to 1.3. Since the carrier turbulent flow is inhomogeneous, such slightly higher concentrations may just be a result of higher particle concentrations in a certain wall-normal location (Costa *et al.* 2016) or in low speed streaks near the channel wall (Shao *et al.* 2012), which does not indicate preferential concentration. In a recent study, Uhlmann & Chouippe (2017) reported the observation of particle clusters in a stationary homogeneous isotropic turbulence with particle Reynolds numbers less than 10 and a particle-to-fluid density ratio of 1.5. In their study, the repulsive barrier was still used. This could indicate that the different observations of particle clusters between the present simulations and Uhlmann's (2008) study are due to both the different particle Reynolds numbers and the use of different lubrication models. Unfortunately, given the lack of reliable experimental benchmark results, the lubrication correction model and its effects require further research. In the remaining part of this paper, all the presented results, i.e. the five cases listed in table 1, are from the simulations with the Stokes lubrication forces. The PLL-RB and PLS-RB cases will not be discussed further.

The shape and the orientation of the particle clusters may also significantly impact the flow modulation. To investigate such aspects, the probability distribution function of the cluster orientation angle θ is calculated for each case. The orientation angle

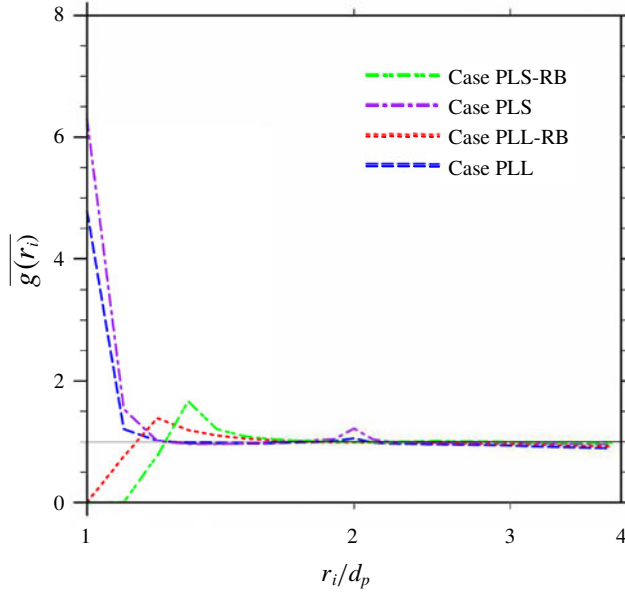


FIGURE 8. (Colour online) Comparison of particle radial distribution functions with different lubrication correction models.

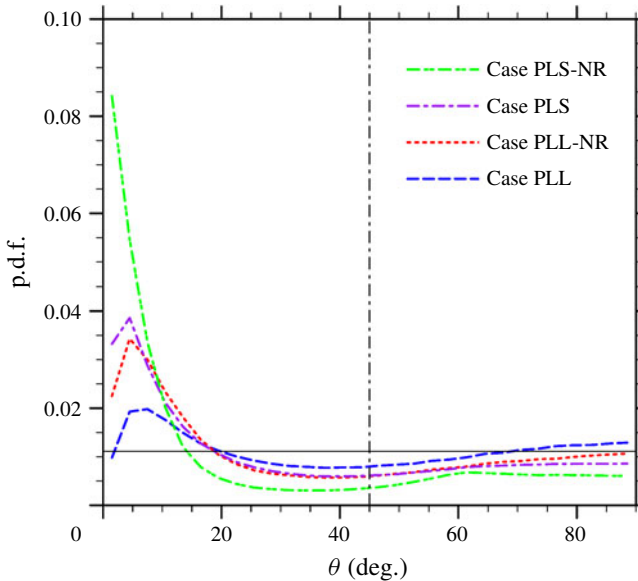


FIGURE 9. (Colour online) The probability distributions of the particle cluster orientation angle θ . Here the bin size is $d\theta = 3^\circ$.

is defined as $\theta = \tan^{-1}(\sqrt{(y_A - y_B)^2 - (z_A - z_B)^2} / \|x_A - x_B\|)$, where (x_A, y_A, z_A) and (x_B, y_B, z_B) are the centre locations of two contacting particles A and B , respectively. When $\theta < 45^\circ$, a particle cluster aligns towards the streamwise direction; when $\theta > 45^\circ$, it aligns towards the cross-streamwise directions. As shown in figure 9, all four cases

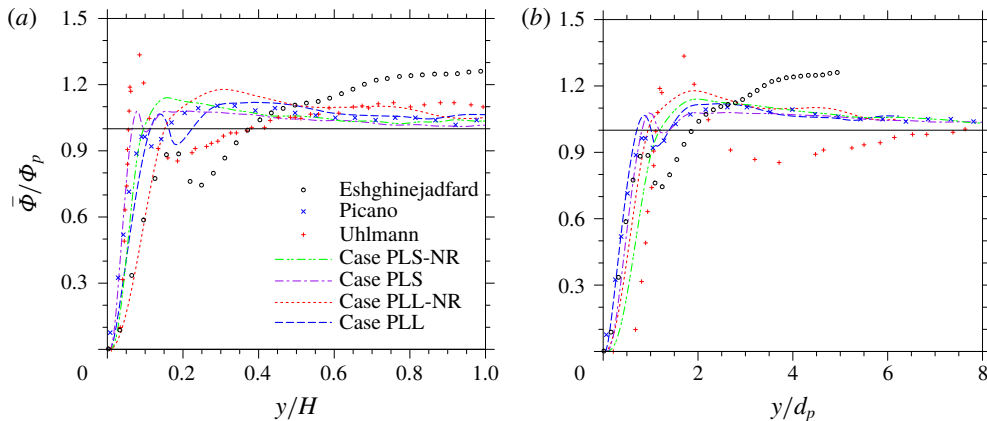


FIGURE 10. (Colour online) The profiles of particle volume fraction as functions of wall-normal locations: (a) wall-normal locations are normalized by the wall unit, (b) wall-normal locations are normalized by the particle diameter. The result of Uhlmann is taken from case B in figure 7 of Uhlmann (2008) with a particle size $d_p/H = 1/20$ and a particle volume fraction $\Phi_p = 0.42\%$. The result of Picano is taken from $\Phi_p = 5\%$ in figure 6(a) of Picano *et al.* (2015) with $d_p/H = 1/9$ and $\Phi_p = 5\%$. The result of Eshghinejadfard is taken from $\Phi_p = 6\%$ in figure 10 of Eshghinejadfard *et al.* (2017) with $d_p/H = 1/5$ and $\Phi_p = 6\%$.

show above-average probabilities (the average probability is shown by the horizontal dash-dot line) for $\theta < 20^\circ$. Particle clusters have the strongest preference to orientate in the streamwise direction in case PLS–NR, followed by case PLS and then case PLL–NR, to the weakest preference in case PLL. An opposite trend is found at large orientation angles. This means clusters of small particles or non-rotating particles have a greater trend to align with the streamwise direction, which agrees well with the visualizations shown in figure 4. There could be multiple explanations why particle clusters preferentially align with the streamwise direction. First, the particle clusters aligned with the streamwise direction bear less shear than those aligned with the cross-streamwise directions. Once a streamwise particle cluster is formed, it has a low probability to be separated. The slip velocity at the contact point of two particles due to the particle rotation also tends to break up a cluster. Compared to the two cases with particle rotation, the two cases where particle rotation is restricted clearly exhibit higher levels of cluster preferential orientation. Second, particle wakes are more likely to stretch in the streamwise direction since the averaged velocities of both the fluid and particle phases are in the same direction. At last, two particles need to have a relative motion to interact with each other, the r.m.s. velocity of the particle phase has the maximum value in streamwise direction.

The particle distribution in the wall-normal direction is also investigated. This distribution is important to understand the local flow modulation at a specific distance from the channel wall. In figure 10 the averaged particle volume fraction profiles are compared with results reported from other studies. When particle rotation is not restricted, the volume fraction profiles in case PLL and case PLS both show a local maximum near the channel wall, followed by a local minimum further away from the wall. The same particle distribution was also reported by other particle-laden channel flow simulations (Uhlmann 2008; Picano *et al.* 2015; Eshghinejadfard *et al.* 2017).

	Φ_p	d_p/H	y_{max}/H	y_{max}/d_p	y_{min}/H	y_{min}/d_p
Uhlmann (2008)	0.42 %	1/20	~ 0.086	~ 1.719	~ 0.184	~ 3.674
Picano <i>et al.</i> (2015)	5 %	1/9	~ 0.098	~ 0.887	~ 0.118	~ 1.062
Eshghinejadfard <i>et al.</i> (2017)	6 %	1/5	~ 0.173	~ 0.864	~ 0.239	~ 1.197
Case PLL	5 %	0.161	0.137	0.854	0.184	1.146
Case PLS	5 %	0.08	0.077	0.958	0.104	1.292

TABLE 3. Wall-normal locations of local maximum and local minimum points of particle volume fraction distribution in particle-laden turbulent channel flow simulations.

As shown in figure 10(b), when normalized by the particle diameter, the local maxima of particle distribution for different sizes of particles occur at similar locations, so do the local minimum points. The same observation was also made by Costa *et al.* (2016). The wall-normal positions of the local maximum and local minimum points in case PLL and case PLS are listed in table 3, together with those reported in other relevant studies.

On the other hand, when the particle rotation is restricted, the particle volume fraction distributions have no such local minimum. The local maximum of the particle volume fraction corresponds to a location where the lubrication force pushing the particles away from the channel wall (see Hall 1988; Mollinger & Nieuwstadt 1996) is balanced with the lift forces driving the particles towards the channel wall. The lift forces consist of a shear-induced part and a rotation-induced part. Although it is not possible to obtain the analytic expression of those lift forces when the particle Reynolds number is finite, it should be reasonable to argue that the direction of these two lift forces follows

$$\text{sign}(F_{L1}) = \text{sign}(\overline{\langle u \rangle} - \overline{\langle v \rangle}) \text{sign} \left(\frac{d\overline{\langle u \rangle}}{dy} \right), \quad (4.1)$$

and

$$\text{sign}(F_{L2}) = \text{sign}[(\overline{\langle u \rangle} - \overline{\langle v \rangle}) \times \overline{\langle \Omega \rangle}], \quad (4.2)$$

respectively, where $\overline{\langle u \rangle}$ and $\overline{\langle v \rangle}$ are the phase and temporally averaged velocity of the fluid and particle phases, respectively; $\overline{\langle \Omega \rangle}$ is the phase and temporally averaged angular velocity of particles. The two expressions in (4.1) and (4.2) are adopted from the analytic expressions based on Stokes disturbance flow (Saffman 1965). The same argument was made in some earlier studies of lift forces at finite particle Reynolds numbers in terms of the Saffman lift multiplied by empirical functions of particle Reynolds number and shear rate (Mei 1992; Kurose & Komori 1999). When considering the lower half of the channel, the mean shear rate $d\overline{\langle u_x^+ \rangle}/dy$ of the flow is always positive, and the only statistically non-zero particle angular velocity component, $\Omega_z = -0.5d\overline{\langle u_x^+ \rangle}/dy$, is negative, as shown in figure 11. Therefore, the directions of the shear-induced lift force and the rotation-induced lift depend on the sign of $(\overline{\langle u \rangle} - \overline{\langle v \rangle})$. Since the particles in the present simulations have finite sizes and cover a finite flow region, it is difficult to define a ‘particle velocity’ at a particular local wall-normal location. Instead, the difference between the phase-averaged fluid and particle velocity in each case is provided in figure 12. We emphasize that these results should not be interpreted as zero-size particles moving faster or slower than the fluid locally. Near the channel wall, since particles can slip near the channel wall

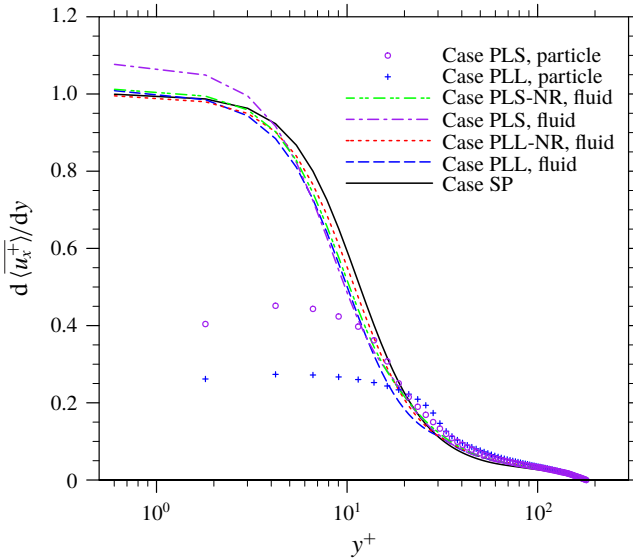


FIGURE 11. (Colour online) Mean velocity gradient in the particle-laden and single-phase turbulent channel flow simulations.

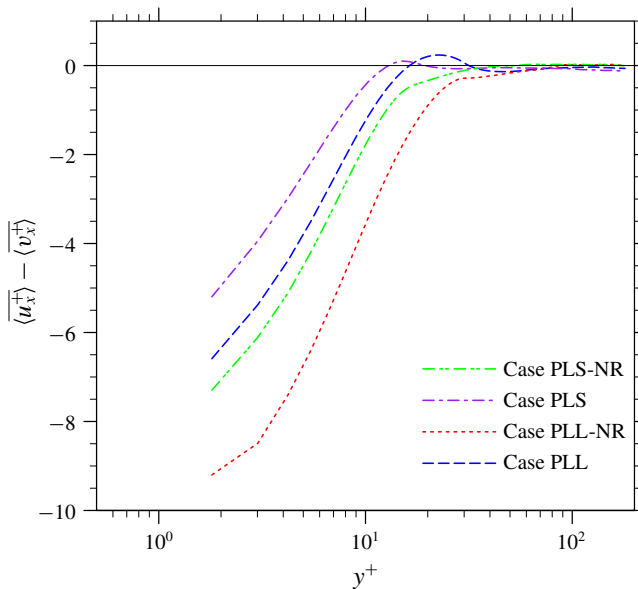


FIGURE 12. (Colour online) The difference between the mean velocities of the fluid and particle phases.

while the velocity of the fluid phase is constrained by the no-slip condition, particles generally move faster than the fluid. Both the average shear-induced lift force and the rotation-induced lift force in this region take a negative value and point to the channel wall. A local maximum point of particle volume fraction therefore is formed

when these two lift forces are balanced by the lubrication force. When the particle rotation is restricted, the particle rotation-induced lift force becomes zero. Thus it is more difficult for particles in case PLL–NR and case PLS–NR to overcome the lubrication force and move close to the channel wall, which explains their smaller particle volume fractions in the near-wall region, and the larger distance of the local maximum point of the particle volume fraction from the wall.

Figure 12 shows that, in case PLL and case PLS, there are small regions where fluid phase moves faster than the particle phase. This may explain the appearance of local minimum points of particle volume fraction in the two cases. Below the wall-normal location of the local minimum, the two lift forces point towards the wall; while above this location, the two lift forces reverse their direction. So the local minimum corresponds to a wall-normal location at which particles are always being pushed away. In case PLL–NR and case PLS–NR, the regions where $\langle \langle u \rangle \rangle > \langle \langle v \rangle \rangle$ disappear, so do the local minimum points in the particle volume fraction profiles. It is worth mentioning that Uhlmann (2008) attributed the appearance of the local minimum points to turbophoresis such that particles tend to migrate from the region with higher turbulence intensity to that with lower turbulence intensity (Reeks 1983). While it is hard to exclude the contribution of turbophoresis, the results obtained from the present simulations cast some doubts on this deduction, since in case PLL–NR and case PLS–NR the condition for turbophoresis would still exist but no local minimum point in the particle volume fraction is observed. It is also difficult to explain that the local minimum points of different sizes of particles happen at different wall-normal locations, while the maximum point of TKE occurs roughly at the same wall-normal location. Another piece of evidence was also reported by Kajishima *et al.* (2001). Their simulations of particle-laden turbulent flow in a vertical channel without particle rotation show that no local minimum point was found in their particle volume fraction profile. Outside the buffer region, the velocity difference between the particle and fluid phases is very small. The lift force is weak accordingly. The profiles of particle volume fraction are rather uniform with a slight downward slope. The same trend was reported by Picano *et al.* (2015), which differs from those observed by Uhlmann (2008), Wang *et al.* (2016b), Eshghinejadfard *et al.* (2017). Interestingly, both the present study and the work of Picano *et al.* (2015) use a physical lubrication force combined with a soft-sphere collision to treat the particle–wall and particle–particle interactions, while the other three investigations adopted the unphysical repulsive barrier to handle particle–wall/particle–particle interactions. The average particle volume fractions range from 0.42% to 20% in these studies. This implies the methods of treating the unresolved hydrodynamic interactions between solid objects could have already played an important role in the dynamics of the particle motion. A careful investigation of this topic is needed, but it is beyond the scope of the current study. In the present simulations, we did not include the lubrication force due to particle rotation. The effect of this additional lubrication force requires a careful investigation in the future.

4.2. Flow modulation by particles

4.2.1. The mean flow and Reynolds stress

The discussion now moves to the flow modulations caused by the presence of solid particles in each case. First, the bulk flow speeds in case SP, case PLL, case PLL–NR, case PLS, case PLS–NR, are 15.736 ± 0.027 , 14.771 ± 0.009 , 15.230 ± 0.036 , 15.281 ± 0.019 and 15.058 ± 0.023 , respectively, when normalized by the friction

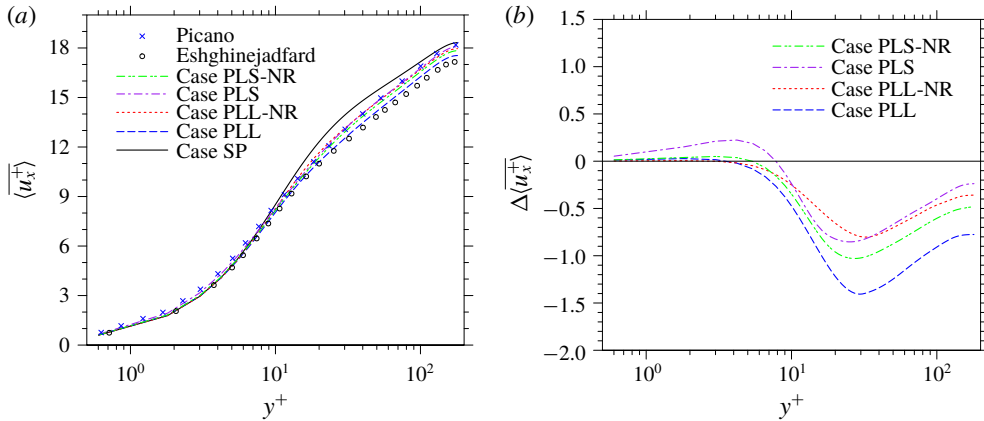


FIGURE 13. (Colour online) The mean flow velocity profiles in the particle-laden channel flow simulations. (a) The mean flow profiles, the result of Eshghinejadfard is taken from figure 5 of Eshghinejadfard *et al.* (2017) for the case with $d_p/H=0.2$, $\Phi_p=6\%$, the result of Picano is taken from figure 3(b) of Picano *et al.* (2015) for the case with $d_p/H=1/9$, $\Phi_p=5\%$ but rescaled. (b) The mean velocity difference between the particle-laden cases and the single-phase case, $\Delta \langle u_x^+ \rangle = \langle u_{x,pl}^+ \rangle - \langle u_{x,sp}^+ \rangle$.

velocity in the unladen case. Hereafter, the value after \pm denotes the standard derivation of an averaged quantity. The mean velocity profiles are compared with these reported in the previous studies of particle-laden channel flows in figure 13. When normalized by the inner scale (friction velocity and wall unit), the mean velocity profiles of case PLS and case PLL are in very good agreement with the results reported by Picano *et al.* (2015) and Eshghinejadfard *et al.* (2017), respectively, when the particle sizes and volume fractions are similar. Unless specified otherwise, the inner scales used for normalization are taken from case SP. The mean velocity profiles in all the particle-laden cases are reduced, compared to the unladen flow, except in the near-wall region.

While the mean velocity profiles of the particle-laden flows were often reported, they had not been well understood. For the sake of discussion, we may express of local fluid velocity in the particle-laden case as

$$\overline{\langle u_x \rangle}_{pl} = \int_0^y \frac{d\overline{\langle u_x \rangle}}{dy'} dy' + \delta u. \quad (4.3)$$

Particles may alter the local mean flow velocity in two ways. On the one hand, particles can directly modify the local fluid velocity through enforcing the no-slip condition on their surface. This mechanism is expressed as a modification δu in (4.3). On the other hand, particles can also modify the local flow velocity by changing the fluid velocity gradient at y' . This mechanism might be pictured as a virtual thin plate that moves with the same speed of the local fluid speed. While the plate does not change the local fluid speed through the no-slip condition, it alters the viscous transport between its two sides, so the velocity gradient $d\overline{\langle u_x \rangle}/dy'$ is modified. The overall modulation of the local fluid velocity is determined by the two mechanisms together.

Correspondingly in the single-phase flow, we have

$$\overline{\langle u_x \rangle}_{sp} = \int_0^y \frac{d\langle u_x \rangle}{dy'} dy'. \quad (4.4)$$

To further demonstrate this, a budget analysis of the streamwise momentum balance at the statistical stationary state in each case is analysed. When the flow reaches a statistical stationary state, the streamwise momentum balance equation of the fluid phase can be obtained as

$$\underbrace{\overline{\langle -u'_x u'_y \rangle}}_{\tau_R} + \underbrace{\frac{1}{\rho} \overline{\langle \alpha \mu \frac{\partial u_x}{\partial y} \rangle}}_{\tau_V} + \underbrace{\frac{1}{\rho} \int_0^y \overline{F_x} dy}_{\tau_P} = \underbrace{\frac{\overline{\tau_{w,pl}}}{\rho} - g \int_0^y \overline{\alpha} dy}_{\tau_T}, \quad (4.5)$$

where α is the volume fraction of fluid phase inside the control volume $V = L_x \times L_z \times \delta y$; $\overline{F_x} = 1/V \int_{S_l \in V} n_j (-p \delta_{xj} + \tau_{xj}) dS$ is the hydrodynamic force in the streamwise direction exerted on the fluid phase by the solid particles, S_l is the fluid–particle interface contained by V ; $\overline{\tau_{w,pl}}$ is the counterpart of mean wall stress $\overline{\tau_w}$ in particle-laden cases. In the present simulation, $\overline{\tau_{w,pl}}$ is obtained by replacing the integration limit y with the half-channel width H in (4.5), i.e. $\overline{\tau_{w,pl}} = \rho g H \Phi_f + \int_0^H \overline{F_x} dy$. The four terms in (4.5) from left to right are given the shorthand notations τ_R , τ_V , τ_P and τ_T , which represent the Reynolds stress, viscous stress, particle-induced stress and the total stress, respectively. The overbar in each term indicates the term is time averaged at the stationary state.

Equation (4.5) in the four particle-laden simulations is examined in figure 14. All terms in (4.5) are explicitly computed with the data obtained in the present simulations. Except case PLS, the other three cases capture well the streamwise momentum balance as the computed left-hand side of (4.5) matches quite well with the computed right-hand side. In case PLS, however, an approximately 8% relative difference between the computed left-hand side and right-hand side is observed at the wall. This deviation is likely due to the insufficient local grid resolution near the channel wall. When a particle is very close to a channel wall, the flow in the gap between the particle surface and the channel wall could be under-resolved. Since particles can have strong slip near the channel wall, a large velocity gradient exists in the gap region between the particle surface and channel wall, which requires higher grid resolutions. The error in case PLS is particularly significant, because this case has the largest particle volume fraction and the largest total particle surface area near the wall, as shown in figure 10. Local grid refinement is needed to improve the results for case PLS. Fortunately, this inadequate grid resolution only affects the small region very close to the channel walls ($y^+ < 5$), and the impact is not as significant in the other three cases. The well-balanced results of different stresses in the other three cases shown in figure 14 can be viewed as a good self-validation to the computed statistics in these simulations.

As discussed earlier, the presence of particles can modify the local mean flow velocity by introducing a non-zero δu in (4.3). This correction term δu is associated with the streamwise particle force, i.e. the force exerted on the fluid phase by particles, $\overline{F_x}^+ = \overline{F_x} \delta y / (\rho u_\tau^2)$, which is shown for each particle-laden case in figure 15. Note that the normalization shown here is different from that used in Yu *et al.* (2017), the latter gave $\overline{F_x} H / (\rho u_\tau^2)$ so the value differs by a factor $H/\delta y$. In the near-wall region $y^+ \leq 10$,

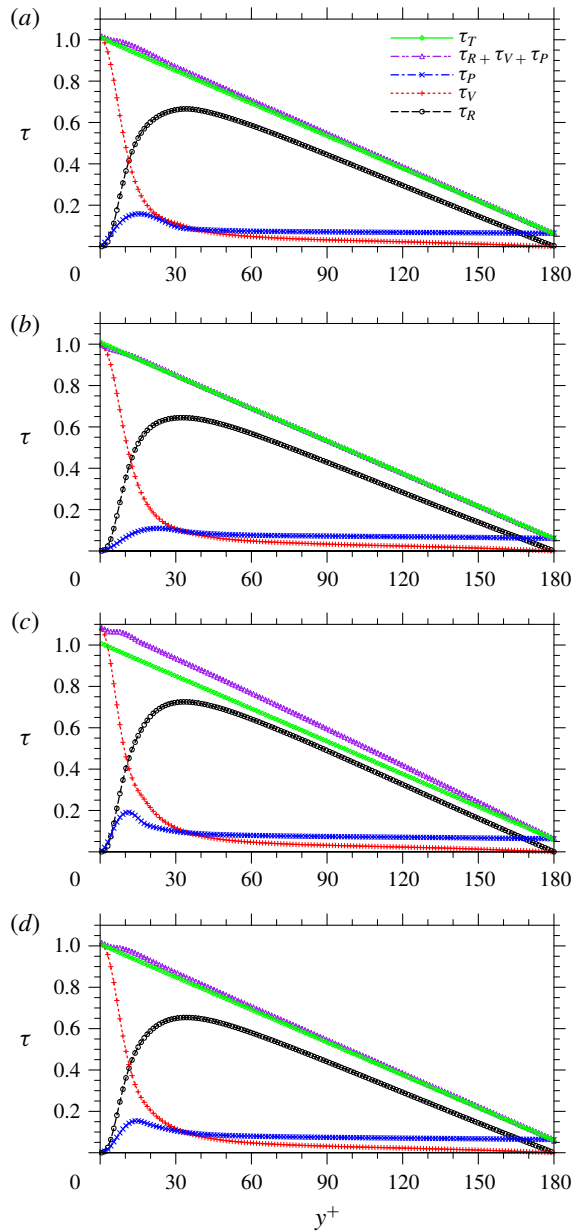


FIGURE 14. (Colour online) The streamwise momentum balance in the particle-laden channel flow simulations: (a) case PLL, (b) case PLL–NR, (c) case PLS, (d) case PLS–NR.

\overline{F}_x in each case is positive, meaning particles push fluid forward. This is because particles can slip on the wall while fluid has to follow the no-slip condition on the wall, thus the particle velocity is much larger than the corresponding fluid velocity. As a result, particles accelerate the fluid velocity locally. Outside the near-wall region, \overline{F}_x in each case changes the sign at some point, which may contribute to the reduced

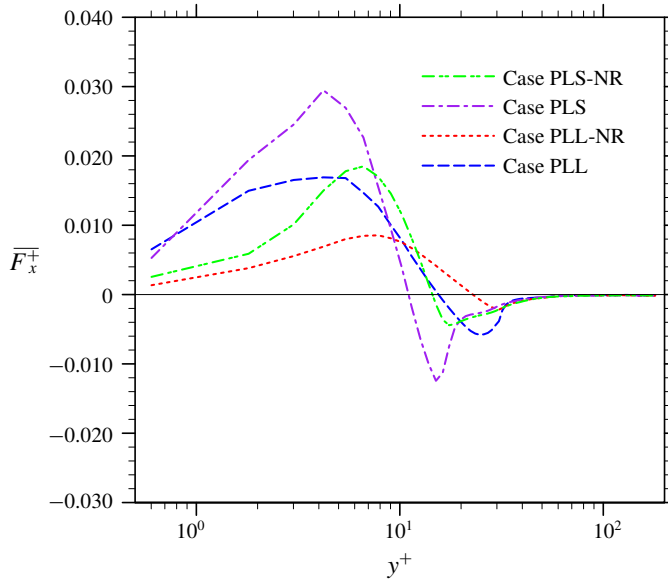


FIGURE 15. (Colour online) Profiles of hydrodynamic force exerted on the fluid phase by particles.

fluid velocity in the particle-laden cases compared to the single-phase case in the same region. It is worth emphasizing that when the velocities of the particle phase and fluid phase are close, the negative particle force \overline{F}_x does not necessarily imply that a faster fluid-phase velocity than the particle-phase velocity, since the results shown in figure 15 are the statistical averages and the local particle force does not scale linearly with the velocity difference in general. However, we do observe that \overline{F}_x is more negative in case PLL and case PLS compared to the corresponding no-rotation cases as the fluid-phase velocities in the former two cases surpass the particle-phase velocities in a small region. Further approaching the channel centre, the hydrodynamic force is almost identically zero, which is probably because the velocities of the particle phase and the fluid-phase converge in the same region, as shown in figure 12.

Besides providing a non-zero particle force to modify the local fluid velocity, the presence of particles also alters the fluid velocity gradient significantly. The profiles of the fluid velocity gradient in the single-phase and particle-laden cases are presented in figure 11. Except in a small region very close to the wall in case PLS, where the accuracy can be affected by the insufficient grid resolution, particles generally reduce the fluid velocity gradient $d\langle u_x \rangle / dy$, as shown in figure 11. Part of the reason is that particles have a much smaller velocity gradient (i.e. twice its spanwise angular velocity) than the velocity gradient of the single-phase channel flow. Very close to the wall, the flow acceleration brought about by the positive particle force could be partially cancelled out by the negative impact due to the reduction of $d\langle u_x \rangle / dy$, but may be still dominating. Thus slightly larger mean flow velocities are observed in the particle-laden cases in this region. A special case happens in case PLS where both mechanisms are positive, thus the flow acceleration is more significant. Outside the viscous sublayer $y^+ \geq 8$, the reduction of $d\langle u_x \rangle / dy$ starts to dominate, thus reduced local fluid velocities compared to the single-phase case are observed. Near the channel centre, the fluid velocity gradient $d\langle u_x \rangle / dy$ in the particle-laden cases becomes slightly

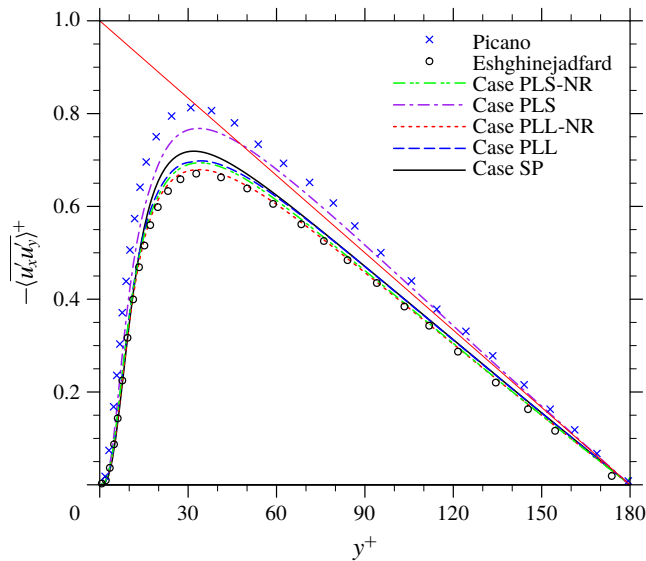


FIGURE 16. (Colour online) The Reynolds stress profiles in single-phase and particle-laden turbulent channel flows. All results are normalized by the inner scale of the corresponding single-phase simulations. The result of Eshghinejadfard is extracted from figure 7 in Eshghinejadfard *et al.* (2017), the result of Picano is extracted from figure 5 in Picano *et al.* (2015) and rescaled.

larger than the single-phase case. Since this phenomenon occurs even in case PLL–NR and case PLS–NR where the velocity gradient of the particle phase is forced to zero, the enhancement of $d\langle u_x \rangle / dy$ is probably because particles enhanced the viscous effect there. Costa *et al.* (2016) argued that, near the channel centre, the particle distribution was rather homogeneous such that the effective viscosity would be enhanced due to the particle suspensions. They proposed a unified log law applicable to both single-phase and particle-laden channel flows, using a rescaling for the latter based on the effective viscosity and the effective distance from the virtual wall formed by local particle concentration, and validated the rescaling against the DNS datasets. We have examined their scaling against our simulation results in both particle-laden turbulent channel and pipe flows (Peng & Wang 2018). Under Costa *et al.*'s (2016) scaling, the slope of the velocity profiles away from the channel wall can be made unified for both single-phase and particle-laden turbulent channel flows. Here we focus on understanding how certain local modulation of the mean flow velocity happens, so the similar investigation is not repeated.

The Reynolds stress profiles of the single-phase and particle-laden simulations are presented in figure 16. In comparison to the Reynolds stress in case SP, the small particles in case PLS result in larger Reynolds stress while the large particles in case PLL lead to smaller Reynolds stress. This particle size dependence was also observed in previous simulations by Shao *et al.* (2012) and Eshghinejadfard *et al.* (2017). Note that in figure 16, the Reynolds stress of Picano *et al.* (2015) is quantitatively larger than that in case PLS because the total driving force was increased in their simulations, but it is unchanged in the present simulations. When particle rotation is restricted, the magnitude of Reynolds stress decreases relative to the corresponding unrestricted case, as shown in figure 16. This comparison reveals two opposite effects

	$\overline{\langle k^+ \rangle}$	$\overline{\langle k_x^+ \rangle}$	$\overline{\langle k_y^+ \rangle}$	$\overline{\langle k_z^+ \rangle}$
Case SP	1.792 ± 0.066	1.176 ± 0.048 (65.6 %)	0.242 ± 0.016 (13.5 %)	0.374 ± 0.021 (20.9 %)
Case PLL	1.663 ± 0.055	1.049 ± 0.038 (63.1 %)	0.231 ± 0.012 (13.9 %)	0.383 ± 0.015 (23.0 %)
Case PLL–NR	1.633 ± 0.087	1.054 ± 0.060 (64.5 %)	0.218 ± 0.014 (13.3 %)	0.361 ± 0.019 (21.1 %)
Case PLS	1.821 ± 0.080	1.152 ± 0.058 (63.3 %)	0.251 ± 0.014 (13.8 %)	0.418 ± 0.018 (23.0 %)
Case PLS–NR	1.662 ± 0.064	1.087 ± 0.041 (65.4 %)	0.215 ± 0.016 (12.9 %)	0.360 ± 0.021 (21.7 %)
	$-\overline{\langle \varepsilon^+ \rangle} \times 10^{-2}$	$-\overline{\langle \varepsilon_x^+ \rangle} \times 10^{-2}$	$-\overline{\langle \varepsilon_y^+ \rangle} \times 10^{-3}$	$-\overline{\langle \varepsilon_z^+ \rangle} \times 10^{-3}$
Case SP	3.373 ± 0.155	2.292 ± 0.090 (67.9 %)	3.996 ± 0.301 (11.8 %)	6.818 ± 0.472 (20.2 %)
Case PLL	3.527 ± 0.091	2.077 ± 0.050 (58.9 %)	5.419 ± 0.190 (15.4 %)	9.084 ± 0.276 (25.8 %)
Case PLL–NR	3.384 ± 0.124	2.178 ± 0.070 (64.4 %)	4.294 ± 0.231 (12.7 %)	7.765 ± 0.374 (22.9 %)
Case PLS	4.156 ± 0.113	2.357 ± 0.060 (56.7 %)	6.863 ± 0.238 (16.5 %)	11.127 ± 0.357 (26.8 %)
Case PLS–NR	3.451 ± 0.115	2.149 ± 0.061 (62.3 %)	4.600 ± 0.244 (13.3 %)	8.427 ± 0.360 (24.4 %)

TABLE 4. The simulated TKEs and dissipation rates. The values in parentheses represent the relative percentages.

of the solid particles on the modification of Reynolds stress. It is well known from the quadrant analysis in a single-phase turbulent channel flow that the Reynolds stress ($-u'_x u'_y$) has the statistical preference in the second (ejection) and fourth (sweeping) quadrants (Kim, Moin & Moser 1987). When particles are present, on the one hand, due to their finite size, particles can filter out the small-scale fluctuations in the fluid phase. This results in a reduction of Reynolds stress and the reduction scales with the particle size. This effect can be seen from the comparisons between case PLL and case PLS, and between case PLL–NR and case PLS–NR. On the other hand, particle rotation in the spanwise direction induces additional ejection and sweeping events through entraining high speed fluid from the channel centre to the channel wall, and promoting ejection of low speed fluid from the wall. This effect is more significant with small particles, since small particles not only have larger spanwise rotation (see figure 11), but also have a larger total surface area than large particles when the particle volume fractions are the same. This explains the larger drop of Reynolds stress from case PLS to case PLS–NR compared to the drop from case PLL to case PLL–NR.

4.2.2. The TKE profile and budget analysis

The average fluid-phase TKE over the whole channel in each case is listed in table 4, and the profiles of TKE are compared in figure 6. Quantities shown in table 4 have been averaged over both the phase and time. In general, the presence of particles results in more homogeneous TKE distributions in the wall-normal direction, with enhanced TKE in the viscous sublayer and reduced TKE in the buffer region,

compared to the single-phase case. The same observation was also reported in the other studies of particle-laden turbulent channel flow simulations by Picano *et al.* (2015), Wang *et al.* (2016b) and Eshghinejadfard *et al.* (2017). A part of this change is directly related to the particle TKE, which is smaller than the TKE of the fluid phase in most regions except near the wall. This is because the finite size of particles makes them respond less to the rapidly changing small-scale fluctuating motions. The restriction of particle rotation further reduces the TKE in the particle phase, as the whole volume occupied by a particle moves with the same velocity. In the near-wall region, particles have larger TKE than the corresponding fluid phase in all four cases, due to the no-slip constraint on the channel walls. The lift forces could also lead to stronger fluctuating motions in the wall-normal direction. The modulation of TKE near the channel centre is small. A slightly increased TKE in case PLS and an almost unchanged TKE in the other three cases can be observed. Overall, TKE in case PLS is always larger than that in case PLL for all wall-normal locations. The same observation applies to the comparison between case PLS–NR and case PLL–NR.

In order to find out what mechanisms are responsible for the TKE modulation described above, a budget analysis of TKE in a particle-laden turbulent flow is conducted. Several previous attempts to investigate the full budget equation of TKE suffered from either difficulty in resolving the flow around the particles or accessing the data or both. In the cases where the particles were small compared to the flow structures, the flow was assumed continuous, with an additional term representing the force acting on the particles. The effect of the particles on the fluid TKE is then simplified as the work done by this particle force (e.g. Kulick *et al.* 1994; Li *et al.* 2001). This simple analysis was sometimes extended to the flows laden with large-size particles. For example, Lucci *et al.* (2010) analysed the sign of $\langle f_i u_i \rangle$ in their simulations of a decaying homogeneous isotropic turbulence laden with finite-size heavy particles, where f_i was defined as the local immersed boundary force due to the presence of particles, u_i was the local fluid velocity. They reported that $\langle f_i u_i \rangle$ was positive, i.e. the presence of particles acted as an extra source rather than a sink of the TKE. The major problem of their study is the lack of clear physical interpretation of the coupling term $\langle f_i u_i \rangle$, since f_i is an algorithm generated term according to the immersed boundary method, instead of a term that is physically determined. Full TKE budget analyses in FRSs became possible only recently. Vreman (2016) performed a budget analysis in homogeneous isotropic turbulence with an array of fixed particles. In this study, since the particles were well defined and not changing, TKE budget equations of the single-phase flow could be applied to the coordinate attached to the particles. Vreman (2016) found that the presence of particles triggered the conveyance of TKE from the far field to the particle surfaces to sustain the enhanced dissipation there. Two other relevant studies were reported by Kajishima *et al.* (2001) and Wang *et al.* (2016a). The former was performed in a simulation of particle-laden turbulent flow in a vertical channel with $Re_p \approx 500$, but no details were provided on what the budget equation was and how this equation was examined. The latter effort calculated terms in a budget equation of TKE in coordinates attached to moving particles in particle-laden homogeneous isotropic turbulence. A direct investigation of the TKE budget equations of a fully resolved particle–fluid two-phase system was performed by Santarelli, Roussel & Fröhlich (2016) for a turbulent channel flow laden with small bubbles acting as rigid particles. This effort provided useful data to understand the turbulence modulation by light particles, but only the budget equation of the total TKE was investigated. In an anisotropic turbulent channel flow,

the inter-component TKE transfer could also be affected by the solid particles, which should be studied. Very recently, Vreman & Kuerten (2018) conducted a TKE budget analysis in their simulation of an array of particles moving at a constant velocity in a turbulent channel flow. Their study only involved the budget analysis of the total TKE, but the analysis was performed in both a moving frame attached the particles and a fixed frame attached to the channel wall. Since Vreman & Kuerten (2018) conducted the simulation with an over-set grid and the fluid–particle interfaces were well defined, their results are accurate and provided a lot of insights into the local turbulence modulation near particle surfaces. However, the wall-normal locations of the particles in this study were quite far away from the channel wall ($y^+ = 90$ and 150), the interactions between the particles and the most inhomogeneous and anisotropic near-wall turbulence were not fully explored. du Cluzeau, Bois & Toutant (2019) reported a full TKE budget analysis in a bubbly turbulent channel flow for both the total TKE and component-wise TKE. However, not every term was calculated explicitly in their work, so it is not possible to assess the overall reliability of their budget analysis.

The budget equations in a particle-laden turbulent channel flow can be derived using the theorem of volume averaging (Prosperetti & Tryggvason 2009; Crowe *et al.* 2011) and from the phase-field theory (Kataoka & Serizawa 1989; Vreman & Kuerten 2018). These two methods essentially reach the same budget equations that are expressed as

total:

$$\begin{aligned}
 \frac{\partial}{\partial t} \alpha \frac{1}{2} \langle u'_i u'_i \rangle &= \underbrace{-\alpha \langle u'_x u'_y \rangle \frac{\partial \langle u_x \rangle}{\partial y}}_{E_p} - \underbrace{\frac{\partial}{\partial y} \alpha \frac{1}{2} \langle u'_i u'_i u'_y \rangle}_{E_{TT}} - \underbrace{\frac{1}{\rho} \frac{\partial}{\partial y} \alpha \langle p' u'_y \rangle}_{E_{PT}} + \underbrace{\frac{1}{\rho} \frac{\partial}{\partial y} \alpha \langle \tau'_{iy} u'_i \rangle}_{E_{VT}} \\
 &\quad - \underbrace{\frac{\alpha}{\rho} \left\langle \tau'_{ij} \frac{\partial u'_i}{\partial x_j} \right\rangle}_{E_{VD}} + \underbrace{\frac{\alpha}{\rho} \left(\langle -p \delta_{ij} + \tau_{ij} \rangle \left(\frac{\partial \langle u_i \rangle}{\partial x_j} - \left\langle \frac{\partial u_i}{\partial x_j} \right\rangle \right) \right)}_{E_{IM}} \\
 &\quad + \underbrace{\frac{1}{\rho V} \int_{S_I} n_j (-p \delta_{ij} u_i + u_i \tau_{ij}) dS}_{E_{IW}} - \underbrace{\frac{1}{\rho V} \langle u_x \rangle \int_{S_I} n_j (-p \delta_{xj} + \tau_{xj}) dS}_{E_{IP}}, \tag{4.6a}
 \end{aligned}$$

streamwise:

$$\begin{aligned}
 \frac{\partial}{\partial t} \alpha \frac{1}{2} \langle u'_x u'_x \rangle &= \underbrace{-\alpha \langle u'_x u'_y \rangle \frac{\partial \langle u_x \rangle}{\partial y}}_{E_{Px}} - \underbrace{\frac{\partial}{\partial y} \alpha \frac{1}{2} \langle u'_x u'_x u'_y \rangle}_{E_{TTx}} + \underbrace{\frac{1}{\rho} \frac{\partial}{\partial y} \alpha \langle \tau'_{xy} u'_x \rangle}_{E_{VTx}} \\
 &\quad + \underbrace{\frac{\alpha}{\rho} \left\langle p' \frac{\partial u'_x}{\partial x} \right\rangle}_{E_{PSx}} - \underbrace{\frac{\alpha}{\rho} \left(\left\langle \tau'_{xx} \frac{\partial u'_x}{\partial x} \right\rangle + \left\langle \tau'_{xy} \frac{\partial u'_x}{\partial y} \right\rangle + \left\langle \tau'_{xz} \frac{\partial u'_x}{\partial z} \right\rangle \right)}_{E_{VDx}} \\
 &\quad + \underbrace{\left[\frac{\alpha}{\rho} \langle p \rangle \left\langle \frac{\partial u_x}{\partial x} \right\rangle + \frac{\alpha}{\rho} \langle \tau_{xy} \rangle \frac{\partial \langle u_x \rangle}{\partial y} - \frac{\alpha}{\rho} \left(\langle \tau_{xx} \rangle \left\langle \frac{\partial u_x}{\partial x} \right\rangle + \langle \tau_{xy} \rangle \left\langle \frac{\partial u_x}{\partial y} \right\rangle + \langle \tau_{xz} \rangle \left\langle \frac{\partial u_x}{\partial z} \right\rangle \right) \right]}_{E_{IMx}} \\
 &\quad + \underbrace{\frac{1}{\rho V} \int_{S_I} n_j (-p \delta_{xj} u_x + u_x \tau_{xj}) dS}_{E_{IWx}} - \underbrace{\frac{1}{\rho V} \langle u_x \rangle \frac{1}{\rho V} \int_{S_I} n_j (-p \delta_{xj} + \tau_{xj}) dS}_{E_{IPx}}, \tag{4.6b}
 \end{aligned}$$

transverse:

$$\begin{aligned}
 \frac{\partial}{\partial t} \alpha \frac{1}{2} \langle u'_y u'_y \rangle &= - \underbrace{\frac{\partial}{\partial y} \alpha \frac{1}{2} \langle u'_y u'_y u'_y \rangle}_{E_{TTy}} - \underbrace{\frac{1}{\rho} \frac{\partial}{\partial y} \alpha \langle p' u'_y \rangle}_{E_{PTy}} + \underbrace{\frac{1}{\rho} \frac{\partial}{\partial y} \alpha \langle \tau'_{yy} u'_y \rangle}_{E_{VTy}} \\
 &+ \underbrace{\frac{\alpha}{\rho} \left\langle p' \frac{\partial u'_y}{\partial y} \right\rangle}_{E_{PSy}} - \underbrace{\frac{\alpha}{\rho} \left(\left\langle \tau'_{xy} \frac{\partial u'_y}{\partial x} \right\rangle + \left\langle \tau'_{yy} \frac{\partial u'_y}{\partial y} \right\rangle + \left\langle \tau'_{yz} \frac{\partial u'_y}{\partial z} \right\rangle \right)}_{E_{VDy}} \\
 &+ \underbrace{\left[\frac{\alpha}{\rho} \langle p \rangle \left\langle \frac{\partial u_y}{\partial y} \right\rangle - \frac{\alpha}{\rho} \left(\langle \tau_{xy} \rangle \left\langle \frac{\partial u_y}{\partial x} \right\rangle + \langle \tau_{yy} \rangle \left\langle \frac{\partial u_y}{\partial y} \right\rangle + \langle \tau_{yz} \rangle \left\langle \frac{\partial u_y}{\partial z} \right\rangle \right)}_{E_{IMy}} \right] \\
 &+ \underbrace{\frac{1}{\rho V} \int_{S_I} n_j (-p \delta_{yj} u_y + u_y \tau_{yj}) dS}_{E_{IWy}}, \tag{4.6c}
 \end{aligned}$$

and spanwise:

$$\begin{aligned}
 \frac{\partial}{\partial t} \alpha \frac{1}{2} \langle u'_z u'_z \rangle &= - \underbrace{\frac{\partial}{\partial y} \alpha \frac{1}{2} \langle u'_z u'_z u'_y \rangle}_{E_{TTz}} + \underbrace{\frac{1}{\rho} \frac{\partial}{\partial y} \alpha \langle \tau'_{yz} u'_z \rangle}_{E_{VTz}} \\
 &+ \underbrace{\frac{\alpha}{\rho} \left\langle p' \frac{\partial u'_z}{\partial z} \right\rangle}_{E_{PSz}} - \underbrace{\frac{\alpha}{\rho} \left(\left\langle \tau'_{xz} \frac{\partial u'_z}{\partial x} \right\rangle + \left\langle \tau'_{yz} \frac{\partial u'_z}{\partial y} \right\rangle + \left\langle \tau'_{zz} \frac{\partial u'_z}{\partial z} \right\rangle \right)}_{E_{VDz}} \\
 &+ \underbrace{\left[\frac{\alpha}{\rho} \langle p \rangle \left\langle \frac{\partial u_z}{\partial z} \right\rangle - \frac{\alpha}{\rho} \left(\langle \tau_{xz} \rangle \left\langle \frac{\partial u_z}{\partial x} \right\rangle + \langle \tau_{yz} \rangle \left\langle \frac{\partial u_z}{\partial y} \right\rangle + \langle \tau_{zz} \rangle \left\langle \frac{\partial u_z}{\partial z} \right\rangle \right)}_{E_{IMz}} \right] \\
 &+ \underbrace{\frac{1}{\rho V} \int_{S_I} n_j (-p \delta_{zj} u_z + u_z \tau_{zj}) dS}_{E_{IWz}}. \tag{4.6d}
 \end{aligned}$$

Here, E_p is the production due to mean flow shear, E_{TT} , E_{PT} , E_{VT} are the transport of TKE in the inhomogeneous direction due to turbulence fluctuation, pressure fluctuation and viscous diffusion, respectively; E_{VD} is the viscous dissipation rate; E_{IM} is the change of TKE due to the unsteadiness of the fluid volume fraction in the fixed control volume V , which arises due to the fact that the spatial gradient of a phase-averaged quantity is not equal to the phase average of the spatial gradient of the same quantity. At the statistically stationary stage, the long-time average of E_{IM} should be zero as the long term average of fluid volume fraction in V is constant. Here, E_{IW} is the rate of work done by the particles on the fluid phase; E_{IP} represents the part of E_{IW} contributing to the kinetic energy of the mean flow; $E_{IW} - E_{IP}$ is therefore the part of particle-induced work that modifies TKE. The last three equations are the component-wise TKE budget equation of the streamwise (x), wall-normal (y) and spanwise velocity (z) components, respectively; E_{PSx} , E_{PSy} and E_{PSz} are the inter-component transfer of TKE due to the pressure strain rate coupling in the streamwise, wall-normal and spanwise directions, respectively; α is the volume

fraction of the fluid phase inside the control volume V ; S_i is the fluid–particle interface inside V . In the present particle-laden turbulent channel flow simulations, the control volume V is naturally chosen as thin layers stretching over the two homogeneous directions, i.e. the streamwise and spanwise directions. Therefore, the spatial derivatives of any quantity in the streamwise and spanwise directions are zero, i.e. $\partial\langle\cdots\rangle/\partial x = \partial\langle\cdots\rangle/\partial z = 0$. Furthermore, the fluid shall have zero mean velocity in the wall-normal and spanwise directions, with and without particles. All these trivial terms are already crossed out in the four TKE budget equations in (4.6). After careful cross-examination, equation (4.6) is found to be identical with the budget equation derived by Vreman & Kuerten (2018) with the assumption of constant driven force and the above simplifications. At the statistical stationary state, the time average of the TKE budget equations in (4.6) are investigated.

The time-averaged values of various terms in the total TKE budget equation are presented in figure 17 for all simulated cases, where the solid black line in each plot represents summation of all terms on the right-hand side of (4.6a); E_{IW} and $-E_{IP}$ are combined as E_W for simplicity. The overall balance in each case is well captured except for a significant deviation in a small region very close to the channel wall in case PLL and case PLS. The imbalances are contained in the region $y^+ < 5$, which roughly correspond to the first three grid points from the wall. They are likely numerical errors due to the insufficient local grid resolution very close to the wall. Without particle rotation, the chance that particles enter the near-wall region is much smaller, thus the numerical errors described above might be small. The fact that the whole particle moves with the same translational velocity may also help reduce the numerical error. The imbalances in case PLL–NR and case PLS–NR are therefore much smaller. Keeping these numerical errors in mind, the near-wall results in case PLL and case PLS must be taken as preliminary results.

A significant volume (5%) is occupied by particles in each particle-laden case. To fairly compare the volumetric intensity of each mechanism, results in figure 17 should be scaled by normalizing the time-averaged local fluid volume fraction in each case, which essentially means the phase average, and is expressed by $\langle\cdots\rangle$ in the rest of the paper. For the sake of conciseness in the ongoing discussion, terms in (4.6a) are grouped into three categories. The TKE production E_P and the particle work E_W are discussed together as the TKE source terms; E_{VD} is the viscous dissipation rate that converts TKE into heat, which alone represents the intensity of TKE sink. Finally, E_{TT} , E_{PT} , E_{VT} and E_{IM} are combined as TKE transport along the wall-normal direction due to flow inhomogeneity.

Time-averaged TKE source terms in the single-phase and particle-laden cases are shown in figure 18. In the viscous sublayer $y^+ \leq 8$, $\overline{\langle E_P \rangle}$ is slightly enhanced in case PLS and almost unaltered in the other three cases. By definition, $\overline{\langle E_P \rangle}$ is the product of the Reynolds stress $\overline{\langle -u'_x u'_y \rangle}$ and the mean velocity gradient $d\langle u_x \rangle/dy$. The slight enhancement inside the viscous sublayer in case PLS is a result of the increase of mean velocity gradient in the same region, as shown in figure 11. Again, caution should be taken as this enhancement may not be quantitatively accurate due to inadequate local grid resolution, as discussed earlier. In the other three cases, the Reynolds stress and mean velocity gradient in the viscous sublayer are almost unaltered, so is $\overline{\langle E_P \rangle}$. In the buffer region, $\overline{\langle E_P \rangle}$ is reduced by the presence of particles in all four particle-laden cases. In case PLS, while the mean velocity gradient in the buffer region is reduced by particles, the Reynolds stress is enhanced. Therefore, the reduction of $\overline{\langle E_P \rangle}$ in case PLS is not as significant as in the other three case, where both the Reynolds stress and mean velocity gradient are reduced. The reduction of

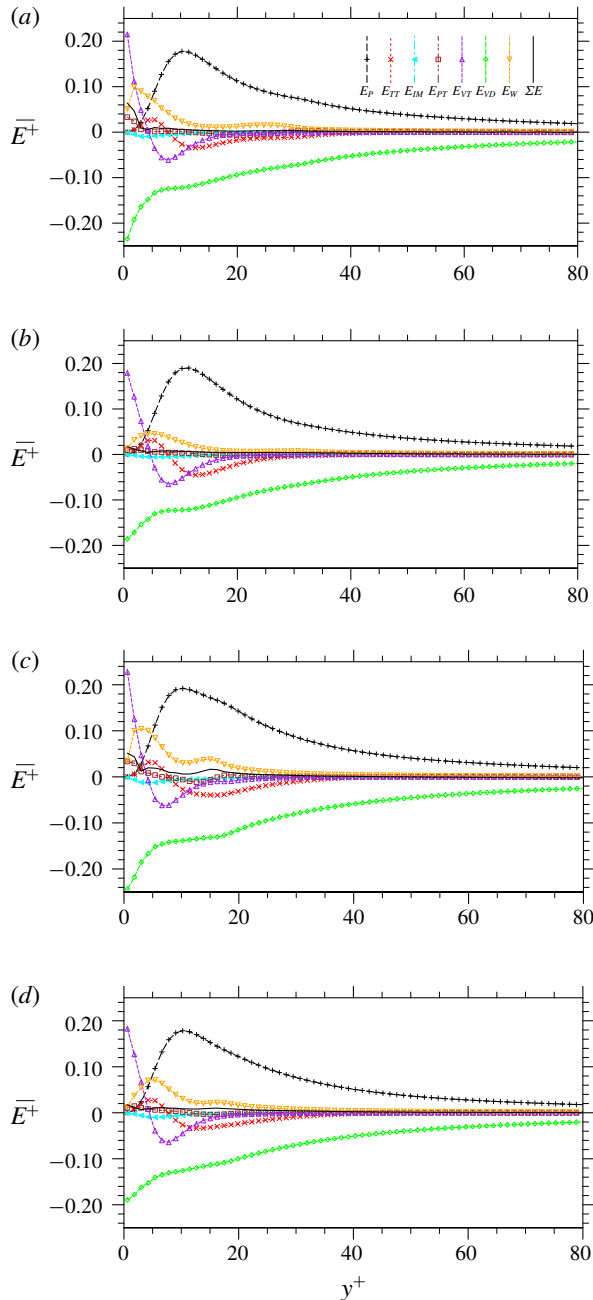


FIGURE 17. (Colour online) Budgets of turbulent kinetic energy in the particle-laden turbulent channel flow simulations: (a) case PLL, (b) case PLL–NR, (c) case PLS, (d) case PLS–NR.

$\overline{E_p}$ in case PLS also occurs over a smaller range of wall-normal locations than these in the other three cases.

Particle rotation can either increase or decrease $\overline{E_p}$ in the buffer region, depending on the particle size. For large particles, although the restriction of particle rotation

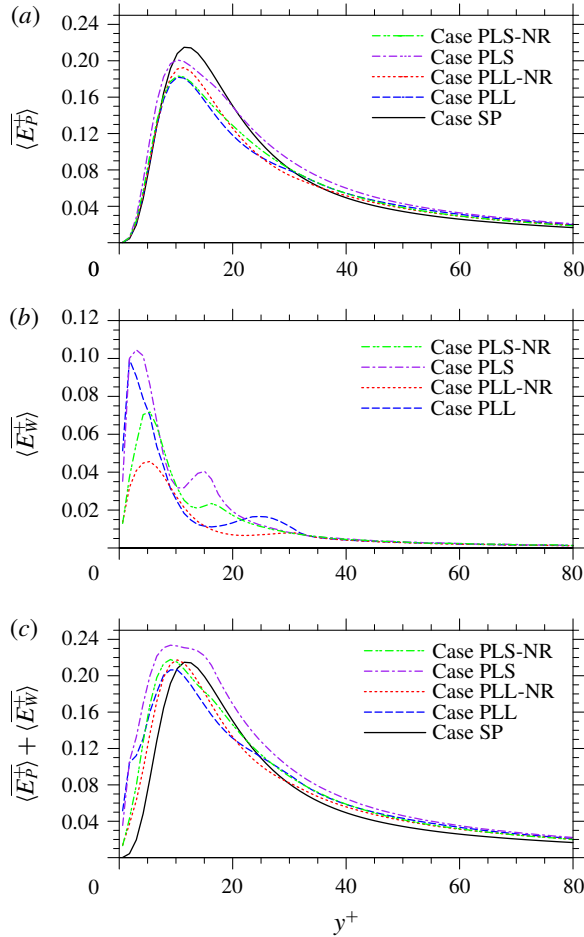


FIGURE 18. (Colour online) Time-averaged rates of TKE input in the single-phase and particle-laden turbulent channel flows. (a) E_p , (b) E_w , (c) $E_p + E_w$.

results in a further reduction of Reynolds stress, it yields a smaller reduction of the mean velocity gradient. The combination leads to a higher $\langle E_p \rangle$ in case PLL–NR than that in case PLL in the buffer region. On the contrary, for small particles, the restriction of particle rotation causes a significant drop of Reynolds stress and almost unaltered mean velocity gradient. Thus a smaller $\langle E_p \rangle$ is observed in case PLS–NR in the buffer region. Moving closer to the channel centre, $\langle E_p \rangle$ is slightly increased in all four particle-laden cases. This change is attributed to the enhanced mean velocity gradient brought by particles, as shown in figure 11. The enhancement in case PLS is greater than the other three cases probably because the Reynolds stress is also increased in this case.

In the present particle-laden flows, particle work E_w always acts as an additional production mechanism of the TKE. The same observation was also made by Lucci *et al.* (2010) in their simulation of decaying homogeneous isotropic turbulence with finite-size particles. In that work, the extra TKE input due to the presence of particles was interpreted as the two-way coupling term $\langle u'f_i \rangle$. As commented earlier, the physical meaning of this two-way coupling term is not as clear as E_w

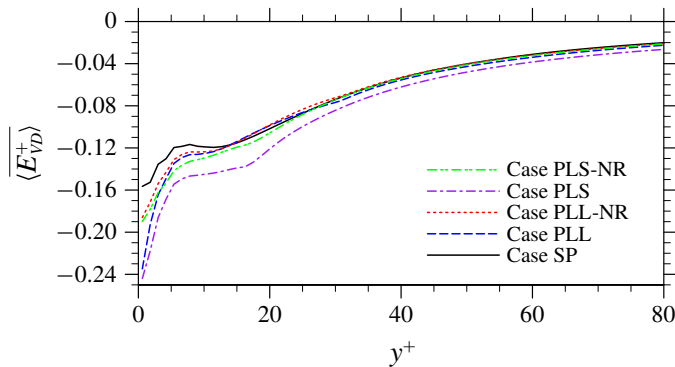


FIGURE 19. (Colour online) Time-averaged rates of viscous dissipation of TKE in the single-phase and particle-laden turbulent channel flows.

derived in the TKE budget. The magnitude of this two-way coupling term also largely depends on the numerical algorithm that defines the coupling force f_i . In the present simulations, E_W contributes to TKE of the fluid phase by either the particle translation or the particle rotation. The comparison of $\overline{\langle E_W^+ \rangle}$ between case PLL(PLS) and case PLL–NR(PLS–NR) in figure 18(b) shows that both mechanisms are important. With the increase of particle size, $\overline{\langle E_W^+ \rangle}$ due to particle rotation takes a larger percentage, which can be seen from the larger drop of $\overline{\langle E_W^+ \rangle}$ in the two large particle cases. This increased importance of particle rotation has two reasons. On the one hand, particle rotation becomes increasingly important when the particle size increase. The effects of particle rotation are usually ignored for small particles. On the other hand, large particles tend to have smaller translational velocity fluctuations than small particles due to their larger size. Comparing the two PLL profiles, there is a small region around $y^+ = 10$ where $\overline{\langle E_W^+ \rangle}$ in the free-rotation case is slightly smaller than that in the corresponding no-rotation case. This is not because particle rotation does negative work on the fluid phase, but rather due to the change of particle distribution when particle rotation is turned off. Unlike the other terms in the budget equations that are essentially volume integrals, E_W is a surface integral that may not be scaled properly by normalizing the fluid volume fraction. The combination of E_P and E_W is the total TKE source. With the addition of E_W , the net TKE input is increased at all wall-normal locations in case PLS, compared to the unladen case. In the other three particle-laden cases, the total rates of TKE input are larger than the unladen case except in the region of $10 \leq y^+ \lesssim 25$.

The time-averaged dissipation rates $\overline{\langle E_{VD} \rangle}$ in different cases are compared in figure 19. The averaged dissipation rate over the whole channel in each case is also listed in table 4. The presence of particles enhances the dissipation rate in case PLS, but has a negligible effect in the other three cases. In the latter three cases, the magnitudes of $\overline{\langle E_{VD} \rangle}$ are increased near the wall at $y^+ \leq 10$, and only marginally altered elsewhere. It should be clear that at the stationary stage, the local dissipation rate of TKE must balance the local TKE source and the TKE transported from other places. Therefore, the presence of particles does not necessarily lead to an enhanced total dissipation rate, as reported in earlier studies of homogeneous isotropic particle-laden turbulent flows (Burton & Eaton 2005; Lucci *et al.* 2010).

Finally, the TKE transport due to the flow inhomogeneity in the wall-normal direction is examined in figure 20. Compared to the single-phase case, less TKE is

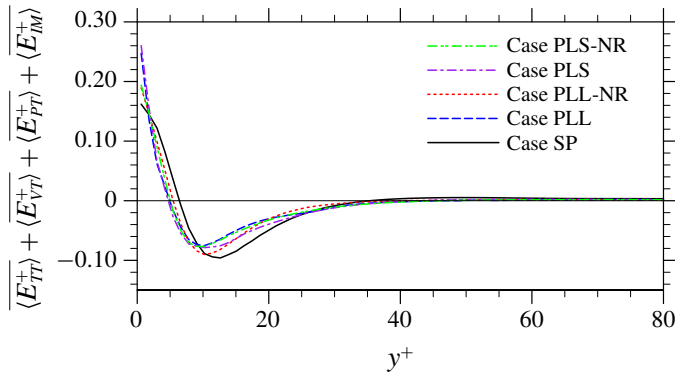


FIGURE 20. (Colour online) Time-averaged rates of turbulent kinetic energy transportation in the single-phase and particle-laden turbulent channel flows.

transported out from $10 \leq y^+ \leq 30$ in the particle-laden cases. As shown in figure 17, the TKE transport in this region is mainly contributed by the turbulent transport E_{TT} , which is suppressed in the particle-laden cases due to the local reduction of turbulence intensity. Very close to the wall $y^+ \leq 2$, more TKE is transported to this region to balance the enhanced viscous dissipation. In this near-wall region, most TKE is transported through viscous diffusion, as the viscous effect dominates locally. The viscous effect in this region is further enhanced by the presence of particles. Since the restriction of particle rotation makes it harder for particles to approach the channel walls, the enhancements of TKE transport in $y^+ \leq 2$ are smaller in cases PLL-NR and PLS-NR, compared to the two freely rotating particle cases. In the region of $2 \leq y^+ \leq 10$, the TKE transport is still mainly carried by the viscous diffusion, as shown in figure 17. The intensity of TKE transport in the particle-laden cases is either reduced ($2 \leq y^+ \leq 5$) or enhanced ($5 \leq y^+ \leq 10$) compared to unladen case, but the overall effect of particles is to reduce the net TKE received by this region. This implies that particles may have two opposite impacts on the overall viscous transport in this region. On the one hand, the presence of particles always enhances the effective viscosity. On the other hand, particles also increase the homogeneity of TKE distribution in the wall-normal direction, which lowers the transport along the wall-normal direction. The contribution of $\langle E_{IM} \rangle$ to the TKE transport is almost negligible. This is expected since although the instantaneous TKE transport due to the dynamic redistribution of particles is non-zero, the long-term average of $\langle E_{IM} \rangle$ should be zero as there is no net particle volume flux in the wall-normal direction.

So far, each mechanism in the budget equation of the total TKE has been quantified using the DNS data. This analysis provides a better understanding of the TKE modulations by the particles. However, it must be emphasized that terms the budget equation only represent the changing rates of TKE instead of TKE itself. An increased rate of TKE production does not necessarily lead to the same increase on TKE itself. The budget analysis based on the statistically stationary condition may also be insufficient to reveal how a new equilibrium state of TKE is established after particles are released. Further insights could be drawn if the dynamic transition from the stationary state of single-phase flow to that of particle-laden flow is examined, which could be a subject for future study. Based on the above analysis, the reduction of turbulent intensity in the region $5 \leq y^+ \leq 30$ in the particle-laden cases is probably due to the reduced TKE production by the flow shear, i.e. E_P , resulting from the

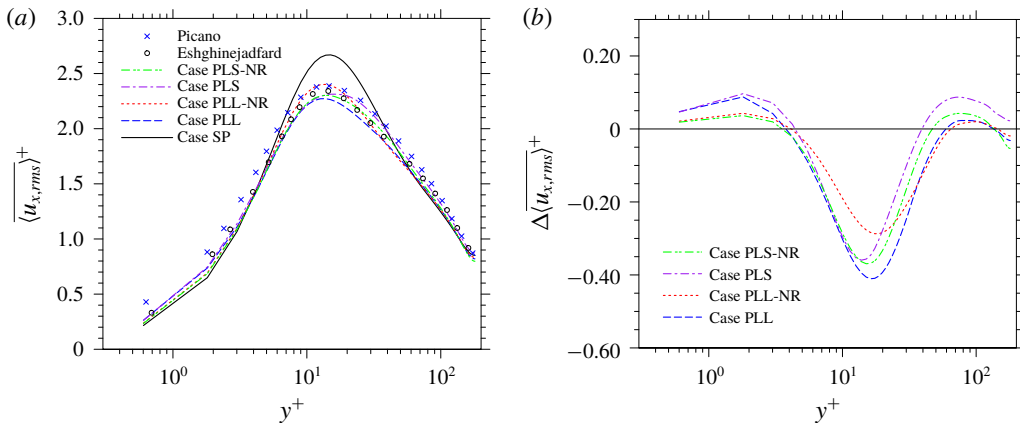


FIGURE 21. (Colour online) The profiles of phase-partitioned streamwise r.m.s. velocity in single-phase and particle-laden turbulent channel flows: (a) streamwise r.m.s. velocity, (b) the modulation of the fluid streamwise r.m.s. velocity compared to single phase. The result of Eshghinejadfard is extracted from figure 6 in Eshghinejadfard *et al.* (2017), the result of Picano is extracted from figure 5 in Picano *et al.* (2015).

reduced mean velocity gradient in the same region, with an exception in case PLS. A same observation was made in the earlier experimental investigation of a turbulent channel flow laden with small particles by Paris (2001), where TKE was found to be significantly reduced while the dissipation rate was only slightly enhanced. In case PLS, on the other hand, adding the particle work E_W , the net TKE production becomes larger compared to that in the single-phase case. In this case, the attenuated TKE in the region of $5 \leq y^+ \leq 30$ might be associated with the enhanced dissipation induced by particles.

4.2.3. The r.m.s. velocities and the budget analyses of component TKEs

Besides the modulation of the total TKE, it is also interesting to investigate how the presence of particles redistributes TKE among different spatial directions. The component-wise TKE averaged over the whole channel in each case is shown in table 4. When particle rotation is not restricted, small particles tend to yield a larger r.m.s. velocity than the large particles in each spatial direction. Such a particle-size effect is much weaker for non-rotating particles. The presence of freely rotating particles also generates a net flux of TKE from the streamwise velocity component to the spanwise component. The same trend is less obvious for non-rotating particles. The profiles of the streamwise, wall-normal and spanwise r.m.s. velocities, computed as $\sqrt{\langle u_x^2 \rangle}$, $\sqrt{\langle u_y^2 \rangle}$, $\sqrt{\langle u_z^2 \rangle}$, respectively, in the single-phase and particle-laden cases are presented in figures 21–23, respectively. These results obtained in the present simulations are in good qualitative agreement with those reported in earlier studies of Picano *et al.* (2015) and Eshghinejadfard *et al.* (2017). Similar to the effect on total TKE, particles generally result in a more uniform streamwise TKE distribution along the wall-normal direction. For the other two velocity components, the presence of particles enhances the TKE near the channel wall but attenuates the TKE near the channel centre, with an exception of case PLS where the wall-normal and spanwise TKEs are enhanced everywhere. As we shall see shortly, this exception is probably

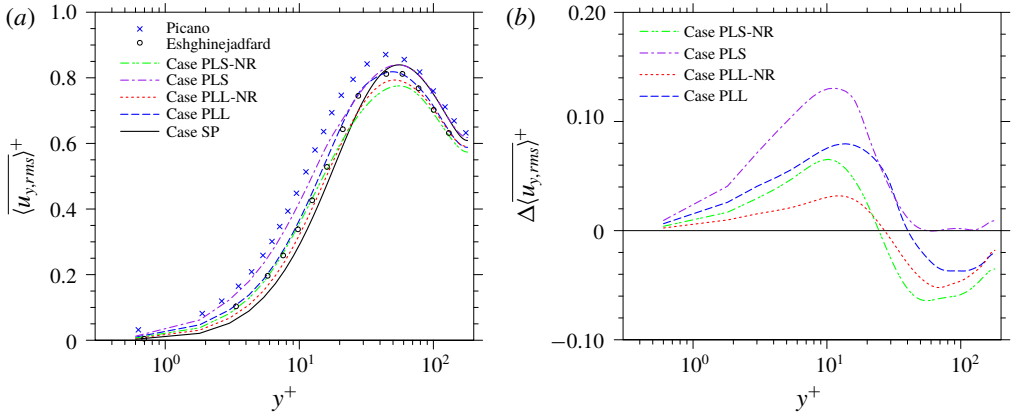


FIGURE 22. (Colour online) The profiles of phase-partitioned wall-normal r.m.s. velocity in single-phase and particle-laden turbulent channel flows: (a) wall-normal r.m.s. velocity, (b) the modulation of the fluid wall-normal r.m.s. velocity compared to single phase. The result of Eshghinejadfard is extracted from figure 6 in Eshghinejadfard *et al.* (2017), the result of Picano is extracted from figure 5 in Picano *et al.* (2015).

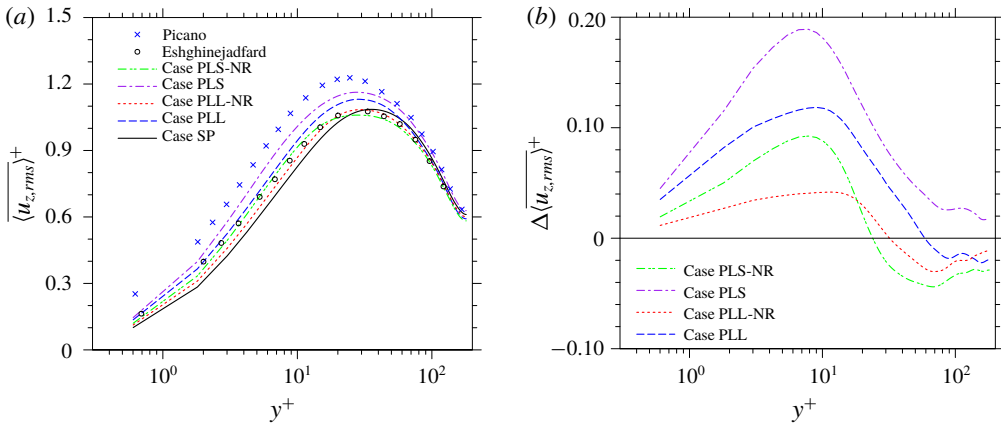


FIGURE 23. (Colour online) The profiles of phase-partitioned spanwise r.m.s. velocity in single-phase and particle-laden turbulent channel flows: (a) spanwise r.m.s. velocity, (b) the modulation of the fluid spanwise r.m.s. velocity compared to single phase. The result of Eshghinejadfard is extracted from figure 6 in Eshghinejadfard *et al.* (2017), the result of Picano is extracted from figure 5 in Picano *et al.* (2015).

related to the strongest enhancement of the inter-component TKE transfer from the streamwise velocity component to the other two velocity components near the channel centre in case PLS compared to other cases.

To better understand the above modulations, the component-wise TKE budget equations, equation (4.6b)–(4.6d), are examined in figures 24–26, respectively. The overall balance shown in (4.6b)–(4.6d) is well captured except that, in case PLL and case PLS, certain errors appear on the two node points next to the channel walls, especially in the streamwise and spanwise directions. Again, these errors are likely related to the inadequate grid resolution locally because of the small gap between the

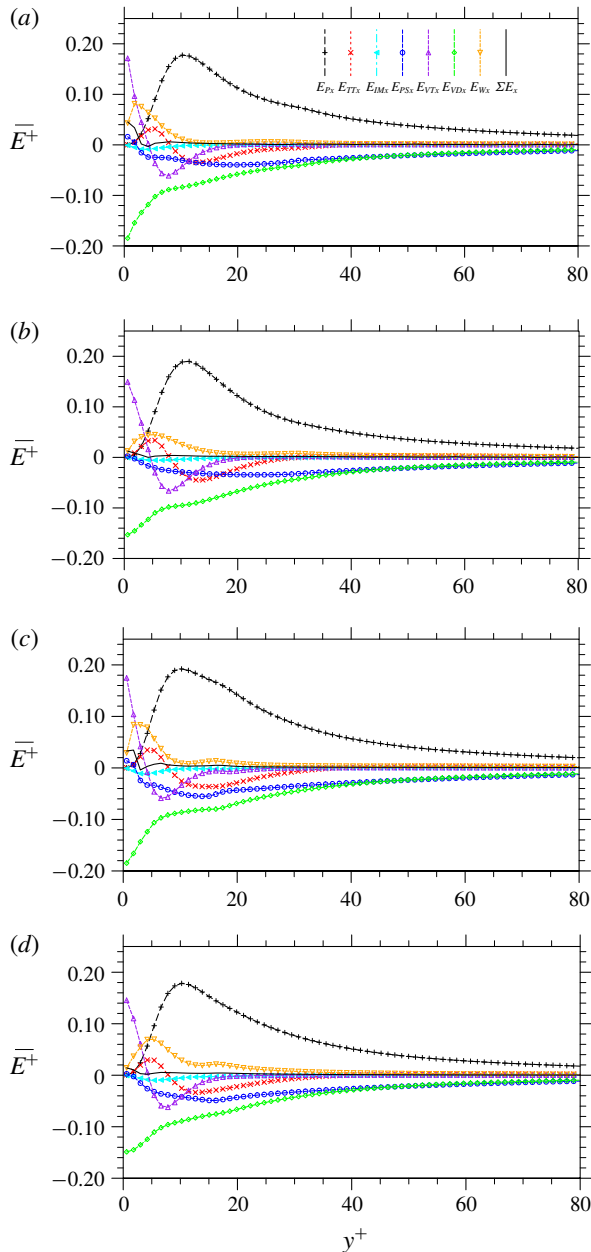


FIGURE 24. (Colour online) Budgets of streamwise turbulent kinetic energy in the particle-laden turbulent channel flow simulations: (a) case PLL, (b) case PLL–NR, (c) case PLS, (d) case PLS–NR.

particles and channel walls. The same errors almost disappear when particle rotation is restricted. For the sake of the simplicity in the following discussion, terms in the TKE budget equations are grouped according to their physical significance. Besides the terms in the budget equation of total TKE, E_{PSi} represents the inter-component transfer of TKE. A positive E_{PSi} indicates the i velocity component is receiving net

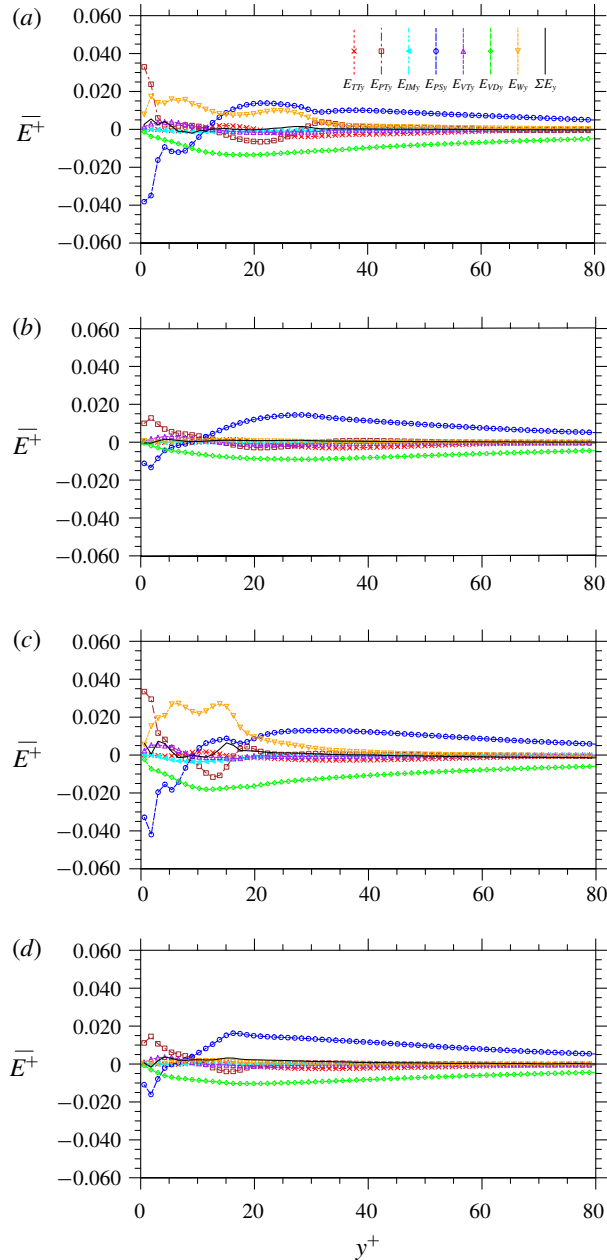


FIGURE 25. (Colour online) Budgets of wall-normal turbulent kinetic energy in the particle-laden turbulent channel flow simulations: (a) case PLL, (b) case PLL–NR, (c) case PLS, (d) case PLS–NR.

TKE from other velocity components. A negative E_{PSi} means the TKE in the i th velocity component is being transferred out to other components.

The time-averaged profiles of the source, the transport, the inter-component transfer and the sink of the streamwise TKE in the single-phase and particle-laden flows are presented in figure 27. In all four particle-laden cases, particle work E_{Wx} serves as an

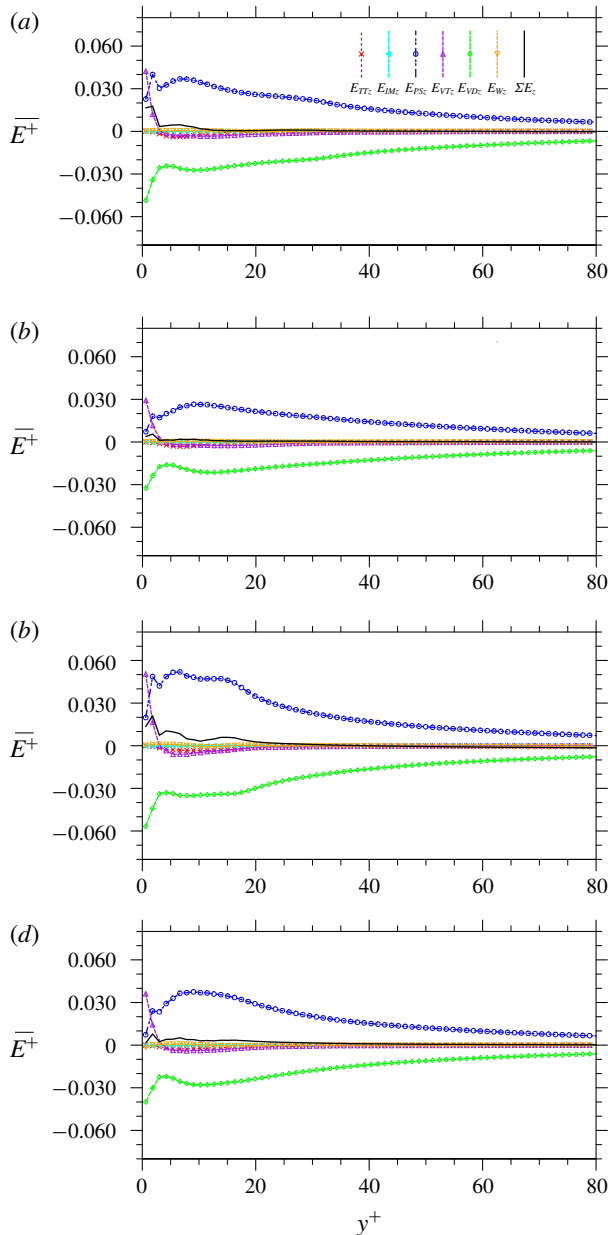


FIGURE 26. (Colour online) Budgets of spanwise turbulent kinetic energy in the particle-laden turbulent channel flow simulations: (a) case PLL, (b) case PLL–NR, (c) case PLS, (d) case PLS–NR.

additional source of TKE throughout the channel. This additional TKE production is contributed by both the translational velocity fluctuation and rotation of the particles. Although E_{Wx} provides additional TKE input, it is not enough to compensate the reduction of E_P in the buffer region, which is due to the reduced flow shear rate. This leads to the attenuation for the streamwise r.m.s. velocity in the same region. The TKE source at other wall-normal locations is, however, increased by the presence

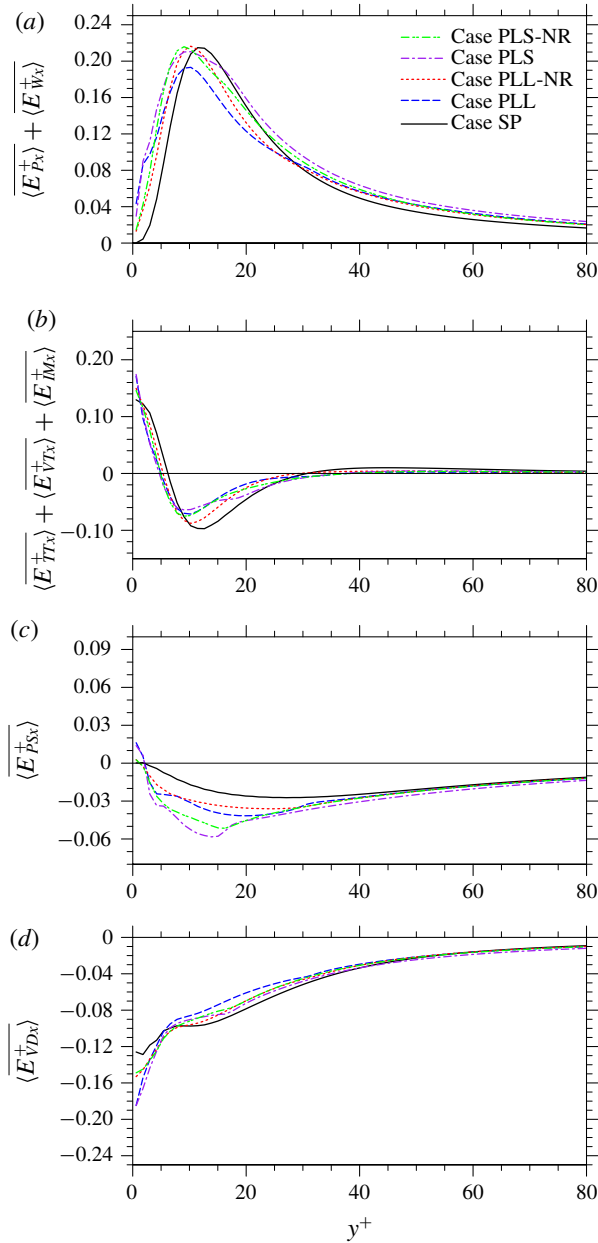


FIGURE 27. (Colour online) Terms in the streamwise turbulent kinetic energy budget equation (4.6b): (a) source, (b) transport, (c) inter-component transfer, (d) viscous dissipation.

of particles. This causes augmentation of the streamwise r.m.s. velocity in the viscous sublayer and outside the buffer region relative to the value in case SP, as shown in figure 21(b). The modification of the streamwise TKE transport is similar to that observed for the total TKE. In the region $10 \leq y^+ \leq 30$ where the turbulent transport $E_{T_{Tx}}$ serves as the major mechanism, less streamwise TKE is transported out because of the reduced turbulence intensity there. Further close to the channel walls, the

viscous transport E_{VT} dominates, and the intensity of the transport of streamwise TKE can be either enhanced ($y^+ \leq 2$ and $5 \leq y^+ \leq 10$) or attenuated ($2 \leq y^+ \leq 5$), probably due to the dual effects of particles on the viscous diffusion, i.e. particles result in larger effective viscosity but at the same time create a more homogeneous distribution of TKE.

The inter-component transfer of TKE is significantly enhanced by the presence of particles. More TKE is given out by the streamwise velocity component to the other two components in both the viscous sublayer and the buffer region, except a small region attached to the wall, as shown in figure 27(c). The strengthened inter-component transfer of TKE results from not only the spherical shape of the particles but also the particle rotation. It eventually leads to a more isotropic TKE distribution in the particle-laden cases in the buffer region. In a small region attached to the channel walls, the streamwise velocity component actually receives net TKE from the other two components when particle rotation is allowed. This phenomenon is not observed in the single-phase case and is very weak in case PLL–NR and case PLS–NR. As will become clear later, this phenomenon occurs essentially because more TKE is transferred from the streamwise velocity component to the wall-normal component in the buffer region. Then, through a significantly enhanced pressure transport mechanism, the received TKE in the wall-normal component is carried from the buffer region to the viscous sublayer. When this wall-normal TKE arrives the near-wall region, it is returned back to the streamwise velocity component, so a positive E_{Px} is observed. Finally, the dissipation rates E_{VDx} of streamwise TKE in the particle-laden cases are enhanced in the viscous sublayer but reduced in the buffer region. The modulation of E_{VDx} balances with the modulations of TKE source, transport and inter-component transfer in each particle-laden turbulent flow case.

The detailed investigation of the terms in the budget equation of wall-normal TKE is presented in figure 28. Different from the single-phase case, where the only source of wall-normal TKE is inter-component transferred from the streamwise TKE, in the particle-laden cases, wall-normal velocity fluctuations also receive energy input directly from the particles work E_{Wy} , as shown in figure 28(a). However, unlike E_{Wx} in the streamwise TKE budget equation that is contributed by both particle translational velocity fluctuation and particle rotation, E_{Wy} in the wall-normal TKE balance almost purely comes from the particle rotation. This observation is made since in case PLL–NR and case PLS–NR where particle rotation is restricted, E_{Wy} is almost zero; E_{Wy} in case PLL and case PLS is significant only in the region of $y^+ \leq 40$. As shown in figure 28(c), in the region of $10 \leq y^+ \leq 30$, particles also enhance the inter-component transfer mechanism and convert more TKE to the wall-normal velocity component. The above two modulations together result in an enhanced wall-normal r.m.s. velocity in the buffer region. Since the transport mechanisms, especially the pressure transport E_{PTy} are significantly augmented, the received wall-normal TKE in the buffer region is transported to the viscous sublayer, as shown in figure 28(b). The enhanced wall-normal TKE transport mechanisms are mainly related to the particle rotation, probably associated with the sweeping events created by the particle rotation. When the particle rotation is restricted, the profiles of TKE transport rates for case PLL–NR and case PLS–NR in figure 28(b) appear similar to that of the single-phase case. When the transported TKE reaches the channel walls, it is transferred to the streamwise and spanwise components rather than dissipated directly into heat, as the dissipation rate of the wall-normal TKE is zero at the wall. The wall-normal TKE transferred back to the streamwise component results in the positive E_{PSx} observed in figure 27(c), while the part of wall-normal

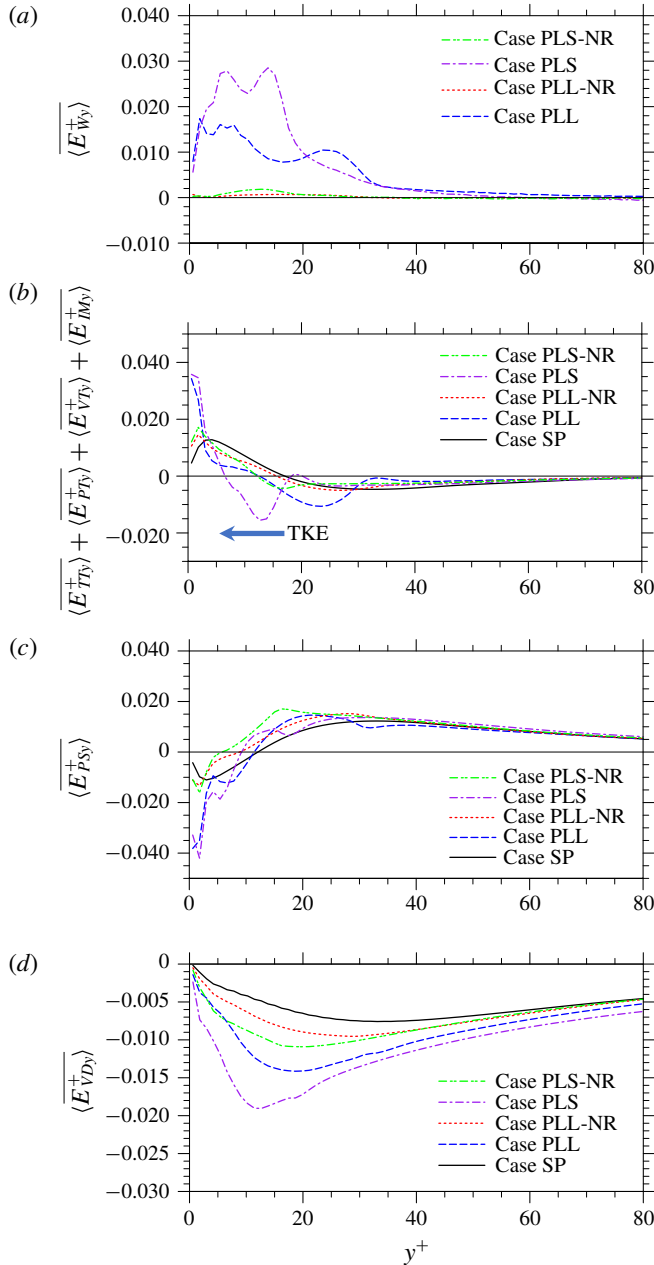


FIGURE 28. (Colour online) Terms in the transverse turbulent kinetic energy budget equation (4.6c): (a) source, (b) transport, (c) inter-component transfer, (d) viscous dissipation.

TKE transferred to the spanwise component further enhanced the spanwise TKE in the near-wall region. At last, the dissipation rates of the wall-normal TKE in the particle-laden cases are significantly enhanced throughout the channel. This can also be seen in table 4. The relative enhancements of $\overline{\langle \varepsilon_y^+ \rangle}$ are 35.6%, 7.5%, 71.7% and 15.1% in case PLL, case PLL–NR, case PLS and case PLS–NR, respectively.

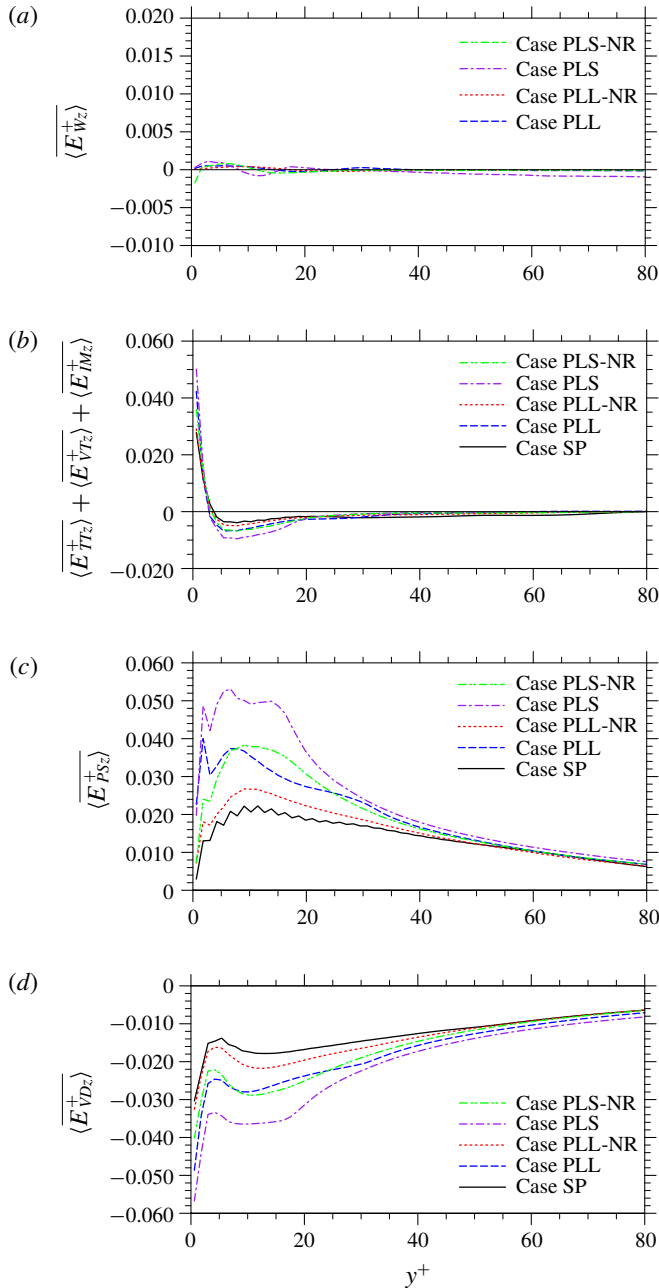


FIGURE 29. (Colour online) Terms in the spanwise turbulent kinetic energy budget equation (4.6d): (a) source, (b) transport, (c) inter-component transfer, (d) viscous dissipation.

Finally, each term in the spanwise TKE budget equation, equation (4.6d), is examined in figure 29. For the spanwise velocity component, the TKE input brought by the particle work E_{Wz} is almost negligible. A nearly zero E_{Wz} together with non-zero E_{Wx} and E_{Wy} implies that only the particle rotation in the spanwise direction

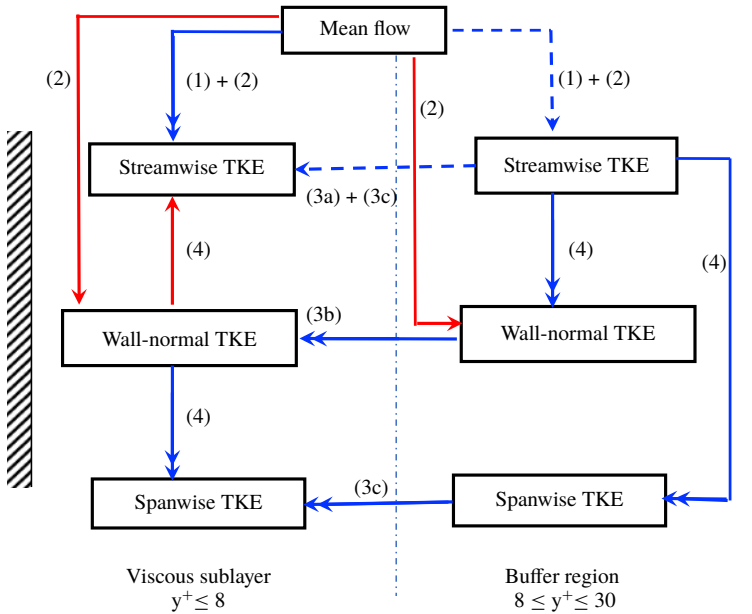


FIGURE 30. (Colour online) Diagram to summarize the results of turbulence modulation by particles from this study. Blue arrows: mechanisms that exist in the single-phase turbulent channel flow, where double arrows represent mechanisms are strengthened by the presence of particles, dash arrows represent mechanisms are weakened by the presence of particles. Red arrows: new mechanisms that are not present in the single-phase turbulent channel flow. Mechanisms: (1) production, (2) particle work, (3a) turbulent transport, (3b) pressure transport, (3c) viscous transport, (4) inter-component transfer.

contributes to the net turbulence modulation. The enhancement of spanwise r.m.s. velocity in the particle-laden cases is due to the enhanced inter-component transfer of TKE from the other two components. This mechanism mainly happens in the region $y^+ \leq 40$, which is in good correspondence with the region of major spanwise r.m.s. velocity enhancement, as shown in figure 23. The zigzag shape of the pressure–strain rate profile in the single-phase case is probably due to the numerical error resulting from the weak compressibility of LBM, which does not affect the conclusions of the budget analyses. The maximum values of $\overline{E_{PS_z}}$ in the particle-laden cases occur around $5 \leq y^+ \leq 20$. This results in an increased level of inhomogeneity that transports more TKE out from $5 \leq y^+ \leq 20$ to $y^+ \leq 5$, in order to balance the enhanced local dissipation in the latter region. Similar to the wall-normal component, the dissipation rate of the spanwise TKE is enhanced throughout the channel in the particle-laden cases.

4.2.4. Summary of TKE modulation by solid particles

The results of various aspects of TKE modulation by solid particles can now be summarized in figure 30. First, the double solid blue arrows represent the existing mechanisms that are strengthened by the presence of particles. These mechanisms include: (1) the inter-component transfer of TKE from the streamwise velocity component to the wall-normal and spanwise components in the buffer region, (2) the production of streamwise TKE from the mean flow in the viscous sublayer, (3)

the pressure transport of the wall-normal TKE from the buffer region to the viscous sublayer, (4) the viscous transport of the spanwise TKE from buffer region to the viscous sublayer, and (5) the inter-component transfer of TKE from the wall-normal component to the spanwise component in the viscous sublayer. Second, the blue dash arrows mark these existing mechanisms that are suppressed by the presence of particles. These mechanisms include (1) the production of the streamwise TKE from the mean flow in the buffer region, and (2) the viscous and turbulent transport of streamwise TKE from the buffer region to the viscous sublayer. Finally, the presence of particles also creates new mechanisms that are not present in the single-phase turbulent channel flow; these are labelled with red solid arrows in figure 30: (1) the production of the wall-normal TKE directly from the mean flow through particle work in both the viscous sublayer and buffer region, and (2) the inter-component TKE transfer from the wall-normal component back to the streamwise component very close to the channel wall. The overall effect of all the above modulations is to yield a more homogeneous distribution of TKE in the wall-normal direction, and a slightly more isotropic distribution of TKE among different velocity components. Since more TKE is transferred from the streamwise velocity component to the other two components when particles are present, the overall dissipation rates of the wall-normal and spanwise TKE take a larger percentage of the total dissipation rate, which is evident in table 4.

5. Summary and discussion

In this study, interface-resolved direct numerical simulations based on the lattice Boltzmann method are used to investigate the two-way coupling effects between finite-size particles and a turbulent channel flow. Specific attention is given to the statistical analysis of local particle clusters in the flow, and the modulations induced by the particles on both the mean flow velocity and turbulent intensity. Not only the phenomena of the two-way coupling effects are described and compared carefully with the existing results in the previous investigations, but also these phenomena are better explained through in-depth analyses of the hydrodynamic forces on the particles and the turbulent kinetic energy budget of the fluid phase. The main conclusions of the present study are summarized as follows.

First, under Stokes lubrication corrections, solid particle clusters are observed in all four particle-laden cases in the present study. This differs from previous studies using non-physical repulsive lubrication barriers. Since Stokes lubrication forces resist relative motions and since neutrally buoyant solid particles have a relatively weak inertia, they tend to stay together after near field or contact interactions. The particle clusters are found to have a preference to align in the streamwise direction. The restriction of particle rotation tends to enhance this preference.

Second, when particles are allowed to rotate freely, the particle volume fraction has a local maximum in the near-wall region of the channel, followed by a local minimum further away from the channel wall. The local maximum results from the balance between the strong transverse lubrication force from the channel wall driving particles away, and the lift forces pointing towards the channel wall due to the mean shear flow and particle rotation. The local minimum is found to be related to the sign change of the relative motion between the fluid and particulate phases causing both lift forces to reverse their direction. When the particle rotation is restricted, the lift force due to particle rotation is eliminated, so the local maximum moves further away from the channel wall, and the local minimum also disappears.

Third, under a constant mean pressure gradient or body force, the presence of particles can alter the bulk flow speed through two mechanisms. The first mechanism is due to the no-slip condition on the particle surface via a non-zero particle force. This particle force is found to be positive near the wall (pushing fluid forward), as solid particles can move faster than the fluid phase there, while it is negative in the buffer region (dragging fluid backward). The second mechanism is related to the reduction of the mean flow velocity gradient, which is found to make a negative contribution to the local mean flow, in both the viscous sublayer and the buffer region except in a small region very close to the wall in case PLL. The reductions of mean velocity gradient near the wall is the main reason for the reductions of bulk flow speed in the particle-laden flows.

Fourth, the presence of particles has two opposite effects on the Reynolds stress. On the one hand, due to their finite size, particles tend to have weaker velocity fluctuations than the fluid phase. The Reynolds stress in the ambient fluid around particles is damped by the particles through the no-slip condition. Larger particles cause a larger reduction in the Reynolds stress. On the other hand, particle rotation in the spanwise direction may excite additional ejection and sweeping events enhancing the Reynolds stress. This effect depends on both the particle angular velocity and the total particle surface area, so the rotation of small particles is found to enhance the Reynolds stress more than large particles.

Furthermore, the distribution of fluid TKE per unit volume is flattened by the presence of particles, with reduced peaks in the buffer region, and enhancements in other regions. A similar modulation is also observed for the streamwise TKE in the particle-laden flows. The wall-normal and spanwise TKE, however, are enhanced in both the viscous sublayer and buffer region by the particles. Outside the buffer region, the total TKE and component-wise TKE are not much affected by the particles.

Finally, a complete budget analysis of TKE is conducted to better understand how the production, transport, inter-component transfer and viscous dissipation of TKE are modified by the particles. The key observations from this analysis include:

- (i) For the total TKE, the rate of production due to the mean flow shear is reduced by the particles in the buffer region due to smaller mean velocity gradients in the particle-laden cases. On the other hand, particles directly do work on the fluid phase to help sustain turbulence. This particle work is attributed to both the translational velocity fluctuation and rotation of the particles. Compared to the single-phase case, the TKE transport in the wall-normal direction in particle-laden cases is reduced in the buffer region and a section of viscous sublayer ($2 \leq y^+ \leq 5$), but enhanced in the rest of viscous sublayer ($y^+ \leq 2$ and $5 \leq y^+ \leq 10$). The viscous dissipation rate of TKE is enhanced everywhere in the case of the small freely rotating particles, but it is enhanced in the viscous sublayer in the other three particle-laden cases. The dissipation rate must balance with the rate of TKE input and rate of TKE transported from elsewhere, and as such it is not necessarily always enhanced by the presence of particles.
- (ii) For the streamwise TKE, particles affect the rate of TKE input and TKE transport similarly as the total TKE. In addition, particles also create a larger inter-component transfer rate of TKE from streamwise velocity component to the other two components. This strengthened inter-component transfer of TKE is due to the more isotropic flow structure around the spherical particles, as well as the particle rotation. The above modulations of the TKE input and the TKE inter-component transfer together explain the reduced streamwise TKE in the buffer region. The dissipation rate of streamwise TKE is enhanced in the viscous sublayer while it is reduced in the buffer region by the particles.

- (iii) The enhanced wall-normal TKE in the viscous sublayer and the buffer region in the particle-laden cases mainly reflects two aspects. First, particles directly do work to sustain the wall-normal velocity fluctuations. Unlike the particle work for the streamwise TKE that results from both particle translational velocity fluctuations and particle rotation, the particle work for the wall-normal TKE is almost fully due to the particle rotation. Second, the presence of particles results in a larger inter-component transfer of TKE from the streamwise component in the buffer region. Then an enhanced pressure fluctuation mainly invoked by particle rotation helps transport this TKE to the viscous sublayer, and finally transfers it back to the streamwise velocity component when the transported TKE arrives at the channel wall. The dissipation rate of the wall-normal TKE is enhanced everywhere in all particle-laden cases.
- (iv) Finally, for the spanwise TKE, the additional TKE source due to particle work is very weak, unlike that for the streamwise and wall-normal TKE. This indicates that the particle work is mainly due to the streamwise translational velocity fluctuations and the spanwise rotation of particles. The enhanced spanwise TKE in the viscous sublayer and buffer region due to the particles is attributed to the strengthened TKE transfer from the other two velocity components. Overall the rates of spanwise TKE transport and dissipation are also enhanced by the presence of particles.

The results from the above budget analysis provide insights into understanding the complexities of turbulence modulation by the particles. However, it must be made clear that the modulation of each mechanism in the budget equations may not be mapped directly to the modulation of the overall turbulent intensity. The budget analysis is based on the statistically stationary assumption of the particle-laden flow, and as such it is also inadequate to draw a conclusion on how particles affect the turbulent intensity from the statistical equilibrium of the unladen flow to the equilibrium of the particle-laden flow. A time-dependent budget analysis of such transient flow between the two equilibrium states could be the subject of future work.

Acknowledgements

The authors would like to acknowledge the valuable comments and suggestions provided by Dr J. C. Brändle de Motta from the CORIA Laboratory at the Normandy University in France. Valuable suggestions from the reviewers are also greatly appreciated. This work has been supported by the National Natural Science Foundation of China (91852205 and 91741101), and by the US National Science Foundation (NSF) under grants CNS1513031 and CBET-1706130. Computing resources are provided by Center for Computational Science and Engineering of Southern University of Science and Technology and by National Center for Atmospheric Research through CISL-P35751014, and CISL-UDEL0001.

REFERENCES

- BALACHANDAR, S. & EATON, J. K. 2010 Turbulent dispersed multiphase flow. *Annu. Rev. Fluid Mech.* **42**, 111–133.
- BOTTO, L. & PROSPERETTI, A. 2012 A fully resolved numerical simulation of turbulent flow past one or several spherical particles. *Phys. Fluids* **24** (1), 013303.
- BOUZIDI, M., FIRDAOUSS, M. & LALLEMAND, P. 2001 Momentum transfer of a Boltzmann-lattice fluid with boundaries. *Phys. Fluids* **13** (11), 3452–3459.

- BRADY, J. F. & BOSSIS, G. 1988 Stokesian dynamics. *Annu. Rev. Fluid Mech.* **20** (1), 111–157.
- BRÄNDLE DE MOTTA, J. C., BREUGEM, W.-P., GAZANION, B., ESTIVALEZES, J.-L., VINCENT, S. & CLIMENT, E. 2013 Numerical modelling of finite-size particle collisions in a viscous fluid. *Phys. Fluids* **25** (8), 083302.
- BRÄNDLE DE MOTTA, J. C., COSTA, P., DERKSEN, J. J., PENG, C., WANG, L.-P., BREUGEM, W.-P., ESTIVALEZES, J. L., VINCENT, S., CLIMENT, E., FEDE, P. *et al.* 2019 Assessment of numerical methods for fully resolved simulations of particle-laden turbulent flows. *Comput. Fluids* **179**, 1–14.
- BRÄNDLE DE MOTTA, J. C., ESTIVALEZES, J.-L., CLIMENT, E. & VINCENT, S. 2016 Local dissipation properties and collision dynamics in a sustained homogeneous turbulent suspension composed of finite size particles. *Intl J. Multiphase Flow* **85**, 369–379.
- BREUGEM, W.-P. 2010 A combined soft-sphere collision/immersed boundary method for resolved simulations of particulate flows. In *ASME 2010 3rd Joint US-European Fluids Engineering Summer Meeting Collocated with 8th International Conference on Nanochannels, Microchannels, and Minichannels*, pp. 2381–2392. American Society of Mechanical Engineers.
- BURTON, T. M. & EATON, J. K. 2005 Fully resolved simulations of particle-turbulence interaction. *J. Fluid Mech.* **545**, 67–111.
- CAIAZZO, A. 2008 Analysis of lattice Boltzmann nodes initialisation in moving boundary problems. *Intl J. Comput. Fluid Dyn.* **8** (1–4), 3–10.
- DU CLUZEAU, A., BOIS, G. & TOUTANT, A. 2019 Analysis and modelling of Reynolds stresses in turbulent bubbly up-flows from direct numerical simulations. *J. Fluid Mech.* **866**, 132–168.
- COSTA, P., PICANO, F., BRANDT, L. & BREUGEM, W.-P. 2016 Universal scaling laws for dense particle suspensions in turbulent wall-bounded flows. *Phys. Rev. Lett.* **117** (13), 134501.
- CROWE, C. T., SCHWARZKOPF, J. D., SOMMERFELD, M. & TSUJI, Y. 2011 *Multiphase Flows With Droplets and Particles*. CRC Press.
- EATON, J. K. 2009 Two-way coupled turbulence simulations of gas-particle flows using point-particle tracking. *Intl J. Multiphase Flow* **35** (9), 792–800.
- ELGHOBASHI, S. & TRUESDELL, G. C. 1993 On the two-way interaction between homogeneous turbulence and dispersed solid particles. I. Turbulence modification. *Phys. Fluids* **5** (7), 1790–1801.
- ESHGHINEJADFARD, A., ABDELSAMIE, A., HOSSEINI, S. A. & THÉVENIN, D. 2017 Immersed boundary lattice Boltzmann simulation of turbulent channel flows in the presence of spherical particles. *Intl J. Multiphase Flow* **96**, 161–172.
- FENG, Z.-G. & MICHAELIDES, E. E. 2005 Proteus: a direct forcing method in the simulations of particulate flows. *J. Comput. Phys.* **202** (1), 20–51.
- FENG, Z.-G. & MICHAELIDES, E. E. 2009 Robust treatment of no-slip boundary condition and velocity updating for the lattice-Boltzmann simulation of particulate flows. *Comput. Fluids* **38** (2), 370–381.
- FERRANTE, A. & ELGHOBASHI, S. 2003 On the physical mechanisms of two-way coupling in particle-laden isotropic turbulence. *Phys. Fluids* **15** (2), 315–329.
- GAO, H., LI, H. & WANG, L.-P. 2013 Lattice Boltzmann simulation of turbulent flow laden with finite-size particles. *Comput. Maths. Applics.* **65** (2), 194–210.
- GLOWINSKI, R., PAN, T.-W., HESLA, T. I. & JOSEPH, D. D. 1999 A distributed lagrange multiplier/fictitious domain method for particulate flows. *Intl J. Multiphase Flow* **25** (5), 755–794.
- GORE, R. A. & CROWE, C. T. 1989 Effect of particle size on modulating turbulent intensity. *Intl J. Multiphase Flow* **15** (2), 279–285.
- GUPTA, A., CLERCX, H. J. H. & TOSCHI, F. 2018 Computational study of radial particle migration and stresslet distributions in particle-laden turbulent pipe flow. *Eur. Phys. J. E* **41** (3), 34.
- HALL, D. 1988 Measurements of the mean force on a particle near a boundary in turbulent flow. *J. Fluid Mech.* **187**, 451–466.
- JOSEPH, G. 2003 Collisional dynamics of macroscopic particles in a viscous fluid. PhD thesis, California Institute of Technology, Pasadena, CA.

- KAJISHIMA, T., TAKIGUCHI, S., HAMASAKI, H. & MIYAKE, Y. 2001 Turbulence structure of particle-laden flow in a vertical plane channel due to vortex shedding. *JSME Intl J.* **44** (4), 526–535.
- KATAOKA, I. & SERIZAWA, A. 1989 Basic equations of turbulence in gas–liquid two-phase flow. *Intl J. Multiphase Flow* **15** (5), 843–855.
- KIM, J., MOIN, P. & MOSER, R. D. 1987 Turbulence statistics in fully developed channel flow at low Reynolds number. *J. Fluid Mech.* **177**, 133–166.
- KULICK, J. D., FESSLER, J. R. & EATON, J. K. 1994 Particle response and turbulence modification in fully developed channel flow. *J. Fluid Mech.* **277**, 109–134.
- KUROSE, R. & KOMORI, S. 1999 Drag and lift forces on a rotating sphere in a linear shear flow. *J. Fluid Mech.* **384**, 183–206.
- KUSSIN, J. & SOMMERFELD, M. 2002 Experimental studies on particle behaviour and turbulence modification in horizontal channel flow with different wall roughness. *Exp. Fluids* **33** (1), 143–159.
- LAMMERS, P., BERONOV, K. N., VOLKERT, R., BRENNER, G. & DURST, F. 2006 Lattice BGK direct numerical simulation of fully developed turbulence in incompressible plane channel flow. *Comput. Fluids* **35**, 1137–1153.
- LEGENDRE, D., ZENIT, R., DANIEL, C. & GUIRAUD, P. 2006 A note on the modelling of the bouncing of spherical drops or solid spheres on a wall in viscous fluid. *Chem. Engng Sci.* **61** (11), 3543–3549.
- LI, Y., MCLAUGHLIN, J. B., KONTOMARIS, K. & PORTELA, L. 2001 Numerical simulation of particle-laden turbulent channel flow. *Phys. Fluids* **13** (10), 2957–2967.
- LUCCI, F., FERRANTE, A. & ELGHOBASHI, S. 2010 Modulation of isotropic turbulence by particles of Taylor length-scale size. *J. Fluid Mech.* **650**, 5–55.
- MAXEY, M. R. 2017 Simulation methods for particulate flows and concentrated suspensions. *Annu. Rev. Fluid Mech.* **49**, 171–193.
- MAXEY, M. R. & RILEY, J. J. 1983 Equation of motion for a small rigid sphere in a nonuniform flow. *Phys. Fluids* **26** (4), 883–889.
- MEI, R. 1992 An approximate expression for the shear lift force on a spherical particle at finite Reynolds number. *Intl J. Multiphase Flow* **18** (1), 145–147.
- MOLLINGER, A. M. & NIEUWSTADT, F. T. M. 1996 Measurement of the lift force on a particle fixed to the wall in the viscous sublayer of a fully developed turbulent boundary layer. *J. Fluid Mech.* **316**, 285–306.
- PAN, Y. & BANERJEE, S. 1997 Numerical investigation of the effects of large particles on wall-turbulence. *Phys. Fluids* **9** (12), 3786–3807.
- PARIS, A. D. 2001 Turbulence attenuation in a particle-laden channel flow. PhD thesis, Stanford University, CA.
- PENG, C., GENEVA, N., GUO, Z. & WANG, L.-P. 2018 Direct numerical simulation of turbulent pipe flow using the lattice Boltzmann method. *J. Comput. Phys.* **357**, 16–42.
- PENG, C., TENG, Y., HWANG, B., GUO, Z. & WANG, L.-P. 2016 Implementation issues and benchmarking of lattice Boltzmann method for moving rigid particle simulations in a viscous flow. *Comput. Maths Applics.* **72** (2), 349–374.
- PENG, C. & WANG, L.-P. 2018 Direct numerical simulations of turbulent pipe flow laden with finite-size neutrally buoyant particles at low flow Reynolds number. *Acta Mechanica* **230**, 517–539.
- PICANO, F., BREUGEM, W.-P. & BRANDT, L. 2015 Turbulent channel flow of dense suspensions of neutrally buoyant spheres. *J. Fluid Mech.* **764**, 463–487.
- PROSPERETTI, A. & TRYGGVASON, G. 2009 *Computational Methods for Multiphase Flow*. Cambridge University Press.
- REEKS, M. W. 1983 The transport of discrete particles in inhomogeneous turbulence. *J. Aero. Sci.* **14** (6), 729–739.
- SAFFMAN, P. G. T. 1965 The lift on a small sphere in a slow shear flow. *J. Fluid Mech.* **22** (2), 385–400.
- SANTARELLI, C., ROUSSEL, J. & FRÖHLICH, J. 2016 Budget analysis of the turbulent kinetic energy for bubbly flow in a vertical channel. *Chem. Engng Sci.* **141**, 46–62.

- SHAO, X., WU, T. & YU, Z. 2012 Fully resolved numerical simulation of particle-laden turbulent flow in a horizontal channel at a low Reynolds number. *J. Fluid Mech.* **693**, 319–344.
- SQUIRES, K. D. & EATON, J. K. 1990 Particle response and turbulence modification in isotropic turbulence. *Phys. Fluids* **2** (7), 1191–1203.
- TANAKA, T. & EATON, J. K. 2008 Classification of turbulence modification by dispersed spheres using a novel dimensionless number. *Phys. Rev. Lett.* **101** (11), 114502.
- TANAKA, T. & EATON, J. K. 2010 Sub-Kolmogorov resolution particle image velocimetry measurements of particle-laden forced turbulence. *J. Fluid Mech.* **643**, 177–206.
- TAO, S., HU, J. & GUO, Z. 2016 An investigation on momentum exchange methods and refilling algorithms for lattice Boltzmann simulation of particulate flows. *Comput. Fluids* **133**, 1–14.
- TEN CATE, A., DERKSEN, J. J., PORTELA, L. M. & VAN DEN AKKER, H. E. A. 2004 Fully resolved simulations of colliding monodisperse spheres in forced isotropic turbulence. *J. Fluid Mech.* **519**, 233–271.
- TEN CATE, A., NIEUWSTAD, C. H., DERKSEN, J. J. & VAN DEN AKKER, H. E. A. 2002 Particle imaging velocimetry experiments and lattice-Boltzmann simulations on a single sphere settling under gravity. *Phys. Fluids* **14** (11), 4012–4025.
- TENNETI, S. & SUBRAMANIAM, S. 2014 Particle-resolved direct numerical simulation for gas-solid flow model development. *Annu. Rev. Fluid Mech.* **46**, 199–230.
- UHLMANN, M. 2008 Interface-resolved direct numerical simulation of vertical particulate channel flow in the turbulent regime. *Phys. Fluids* **20** (5), 053305.
- UHLMANN, M. & CHOUPIPE, A. 2017 Clustering and preferential concentration of finite-size particles in forced homogeneous-isotropic turbulence. *J. Fluid Mech.* **812**, 991–1023.
- VREMAN, A. W. 2015 Turbulence attenuation in particle-laden flow in smooth and rough channels. *J. Fluid Mech.* **773**, 103–136.
- VREMAN, A. W. 2016 Particle-resolved direct numerical simulation of homogeneous isotropic turbulence modified by small fixed spheres. *J. Fluid Mech.* **796**, 40–85.
- VREMAN, A. W. & KUERTEN, J. G. M. 2018 Turbulent channel flow past a moving array of spheres. *J. Fluid Mech.* **856**, 580–632.
- WANG, L.-P., ARDILA, O. G. C., AYALA, O., GAO, H. & PENG, C. 2016a Study of local turbulence profiles relative to the particle surface in particle-laden turbulent flows. *J. Fluids Engng* **138** (4), 041307.
- WANG, L.-P., PENG, C., GUO, Z. & YU, Z. 2016b Flow modulation by finite-size neutrally buoyant particles in a turbulent channel flow. *J. Fluids Engng* **138** (4), 041306.
- WANG, L.-P., PENG, C., GUO, Z. & YU, Z. 2016c Lattice Boltzmann simulation of particle-laden turbulent channel flow. *Comput. Fluids* **124**, 226–236.
- WEN, B., ZHANG, C., TU, Y., WANG, C. & FANG, H. 2014 Galilean invariant fluid–solid interfacial dynamics in lattice Boltzmann simulations. *J. Comput. Phys.* **266**, 161–170.
- WU, T., SHAO, X. & YU, Z. 2011 Fully resolved numerical simulation of turbulent pipe flows laden with large neutrally-buoyant particles. *J. Hydrodyn.* **23** (1), 21–25.
- XU, Y. & SUBRAMANIAM, S. 2010 Effect of particle clusters on carrier flow turbulence: a direct numerical simulation study. *Flow, Turbul. Combust.* **85** (3), 735–761.
- YANG, F.-L. & HUNT, M. L. 2006 Dynamics of particle–particle collisions in a viscous liquid. *Phys. Fluids* **18** (12), 121506.
- YU, Z., LIN, Z., SHAO, X. & WANG, L.-P. 2017 Effects of particle-fluid density ratio on the interactions between the turbulent channel flow and finite-size particles. *Phys. Rev. E* **96**, 033102.
- ZENG, L., BALACHANDAR, S., FISCHER, P. & NAJJAR, F. 2008 Interactions of a stationary finite-sized particle with wall turbulence. *J. Fluid Mech.* **594**, 271–305.
- ZHAO, W. & YONG, W.-A. 2017 Single-node second-order boundary schemes for the lattice Boltzmann method. *J. Comput. Phys.* **329** (6), 1–15.